Rapid Analysis of Elemental Impurities in Battery Electrolyte by ICP-OES

Quality control measurement of 12 elements in lithium hexafluorophosphate

Download now

Agilent | Trusted Answers

Highly Stable Quasi-Solid-State Lithium Metal Batteries: Reinforced Li$_{1.3}$Al$_{0.3}$Ti$_{1.7}$(PO$_4$)$_3$/Li Interface by a Protection Interlayer

Zhen Chen, Guk-Tae Kim,* Jae-Kwang Kim,* Maider Zarrabeitia, Matthias Kuenzel, Hai-Peng Liang, Dorin Geiger, Ute Kaiser, and Stefano Passerini*

NASICON-type Li$_{1+x}$Al$_x$Ti$_{2-x}$(PO$_4$)$_3$ (LATP) solid electrolytes have developed as a promising candidate for solid-state lithium batteries. However, the brittle and stiff LATP suffers from poor physical contact with electrodes and chemical/electrochemical instability at electrode|electrolyte interfaces. Herein, a thin and flexible hybrid electrolyte comprised of LATP and poly(vinylidene fluoride-trifluoroethylene) (PVDF-TrFE) incorporated with highly concentrated ionic liquid electrolyte (ILE) is prepared to resolve these prominent limitations. To further protect the LATP|Li interface, an ultrathin poly[2,3-bis(2,2,6,6-tetramethylpiperidine-N-oxycarbonyl)-norbornene] (PTNB) polymer is coated on Li, acting as an additional protective layer. Consequently, the lithium stripping-plating lifetime is prolonged from 128 to 792 h, with no dendritic lithium observed. The PTNB@Li||LiNi$_{0.8}$Co$_{0.1}$Mn$_{0.1}$O$_2$ (PTNB@Li||NCM$_{811}$) cells achieve significantly improved rate capability and cycling stability, predominantly resulting from the drastically decreased interfacial resistances, prohibited dendritic lithium generation, mitigated cathode material phase evolution, and prevention of internal microcrack formation. The thinner interphases formed on NCM$_{811}$ and PTNB@Li electrodes also play a key role. The quasi-solid-state batteries allow for the fabrication of multi-layer bipolar cells with stable cycling. Even under some exertive circumstances, (limited lithium source, low temperature, e.g., 0 °C), the impressive electrochemical performance achieved highlights the importance of such quasi-solid-state lithium batteries as a viable solution for the next-generation high-performance lithium batteries.

1. Introduction

Lithium-ion batteries (LIBs) have been widely used in various energy storage devices including portable electronics, electric vehicles, and grid energy storage systems, owing to their high energy density and long cycling lifetime.[1,2] Unfortunately, the development of LIBs is approaching its bottleneck. Public safety concerns have arisen from frequently reported incidents such as electrolyte leakage, fire, and even explosion,[3–5] which has driven research interests for safer battery systems. To boost transport electrification, the ongoing demands of higher energy/power densities and safety require alternative energy storage systems.[6–8] It was reported that an energy density augment of 40–50% can be achieved simply by replacing graphite with lithium metal,[9,10] the latter is appealing for its extremely high specific capacity (3860 mAh g^{-1}) and low redox potential (−3.04 V vs standard hydrogen electrode (SHE)).[11,12] Apart from high flammability, high volatility, high toxicity, and a narrow operational temperature range, the conventional organic carbonate-based liquid electrolytes show incompatibility with highly reactive metallic lithium through furnishing the notorious dendritic lithium formation and further triggering cell short circuit.[4] Alternatively, solid-state batteries (SSBs) which enable the use of lithium metal as the negative electrode stand out for their inherent distinctive advantages, mainly no electrolyte leakage issues, reduced lithium dendrites growth, environmental friendliness, and wide operational temperature range.[13,14] Furthermore, the implementation of solid

Dr. Z. Chen, Dr. G.-T. Kim, Dr. M. Zarrabeitia, Dr. M. Kuenzel,
H.-P. Liang, Prof. S. Passerini
Helmholtz Institute Ulm (HIU)
89081 Ulm, Germany
E-mail: guk-tae.kim@kit.edu; stefano.passerini@kit.edu

The ORCID identification number(s) for the author(s) of this article can be found under https://doi.org/10.1002/aenm.202101339.

Dr. Z. Chen, Dr. G.-T. Kim, Dr. M. Zarrabeitia, Dr. M. Kuenzel,
H.-P. Liang, Prof. S. Passerini
Karlsruhe Institute of Technology (KIT)
76021 Karlsruhe, Germany

Prof. J.-K. Kim
Department of Energy Convergence Engineering
Cheongju University
Cheongju, Chungbuk 28503, Republic of Korea
E-mail: jaekwang@cju.ac.kr

Dr. D. Geiger, Prof. U. Kaiser
Central Facility of Electron Microscopy
Electron Microscopy Group of Materials Science
Ulm University
Albert-Einstein-Allee 11, D-89081 Ulm, Germany

ADVANCED
SCIENCE NEWS
www.advancedsciencenews.com

ADVANCED
ENERGY
MATERIALS
www.advenergymat.de

electrolytes facilitates the bipolar design which minimizes accessory components associated with electrical connection and battery packaging. This not only reduces the overall fabrication cost, but also increases the energy density because of the decreased weight and volume.[15] The bipolar cells are assembled by directly connecting multi-layers of individual mono-polar unit cells in series to increase the voltage output. As a result, the uniform current/potential distribution over the active surface area with considerably shortened pathways and diminished internal resistances arising from electrical connections contributes to a supplementary boost of power density.[16]

Nevertheless, two common yet critical challenges of SSBs, that is, the interfacial chemical/electrochemical instability and the poor physical contact between solid electrolyte and electrodes, must be eliminated before their commercialization.[14,17] NASICON-type lithium aluminum titanium phosphate $Li_{1+x}Al_xTi_{2-x}(PO_4)_3$ (LATP) has emerged as a promising solid electrolyte candidate. LATP has been intensively studied due to its salient features of high ambient ionic conductivity $(10^{-4}–10^{-3}$ S cm$^{-1})$, wide electrochemical window (>5 V), high thermal stability, high chemical resistance towards air, and the ability for an economical large-scale synthesis with good reproducibility.[18,19] Though, LATP suffers from common limitations like most of the solid electrolytes, such as chemical instability against lithium metal, which causes spontaneous reduction of Ti^{4+} and generates the reactive-type of mixed conducting interphases (MCIs).[20] The latter can potentially foster lithium dendrites formation and growth owing to its ionic/electronic conducting ability. This may cause the internal short circuit of batteries, preventing their wide-scale application. To isolate the direct contact between LATP and lithium metal, strategies such as the surface coating of artificial protective layers including but not limited to metallic film,[21] nanocomposites,[22,23] metal oxides,[24,25] polymers,[26–28] and Li-conductors[29–31] have been proposed. Although the physical contact between LATP and lithium metal has been effectively avoided, the preparation of these protection layers is complicated and time-consuming.

Another issue to overcome is the poor physical contact resulting from the point-by-point contact between LATP and cathode electrode, generating a high polarization due to the decreased Li$^+$ and charge transfer sites.[17] To achieve close contact between cathode and electrolyte, a common strategy is to adopt a co-sintering of ceramic pellet with a thin cathode electrode deposited on one side of the pellet. Nevertheless, the mandatory high temperature to permit grain boundary growth usually sacrifices the chemical stability between LATP and cathode material because of inevitable parasitic reactions.[32]

Researchers have been working on developing quasi-solid-state systems, that is, solid-liquid hybrid electrolyte and polymer-ceramic composite electrolyte. Despite the improved interfacial contact and enhanced mechanical property,[33] the incorporation of the polymer could lower the overall ionic conductivity because of its markedly lower ionic conductivity compared to the oxides-based electrolyte counterpart. What's more, it complicates the Li$^+$ migration in virtue of the discrepancy of Li$^+$ diffusion kinetics across the polymer/ceramic interfaces/interphases.[34,35] On the other hand, although the hybridization of the conventional liquid electrolyte with solid electrolyte would enhance the ionic conductivity, electrolyte wettability, and interfacial contact, it compromises the safety property. It was

reported by Busche et al. that a resistive solid-liquid electrolyte interphase (SLEI) forms when contacting lithium aluminum germanium phosphate with liquid electrolyte (i.e., lithium bis(trifluoromethanesulfonyl)imide (LiTFSI) in 1,3-dioxolane and 1,2-dimethoxyethane (DME)). Such an SLEI can form with minimal contact between a solid and a liquid electrolyte, severely growing in the presence of water.[36] To circumvent these shortcomings, the preparation of a hybrid electrolyte that combines ion-conducting ceramic, electrochemically inactive polymer, and an ionic liquid electrolyte (ILE) appears as a promising strategy.

The ILE exhibits low flammability, negligible vapor pressure, improved thermal stability, and good compatibility with lithium metal, offering an auspicious replacement of organic carbonate-based liquid electrolyte.[4,37–41] In 2018, we reported an outstanding cycling stability (>85% capacity retention for 2000 cycles at 1C) in a lithium battery configuration employing $0.2LiTFSI-0.8Pyr_{14}FSI$ (N-butyl-N-methylpyrrolidinium bis-(fluoromethanesulfonyl) imide) as the alternative ILE.[37] This indicates a high compatibility of ILE with lithium metal. Jeong et al. stated that increasing the Li salt concentration leads to thinner solid electrolyte interphase (SEI) formation, suppressed dendritic lithium formation, and thus improved cyclability.[42] Through atomic force microscopy and molecular dynamics simulations,[43] Rakov et al. confirmed that the high salt concentration in ILE is beneficial for the formation of favorable SEI to ensure no dendrite formation upon cycling, even at high current densities.[44] Poly(vinylidene fluoride-trifluoroethylene) (PVDF-TrFE) is electrochemically inactive polymer and it has a low degree of crystallinity and high dielectric constant ($\varepsilon = \approx12$). The essential characteristics allow an improvement of ionic transfer with lithium-ion mobility due to anion trapping,[45,46] rendering it a good binder for the preparation of flexible membranes. Therefore, here we prepare a thin and flexible hybrid electrolyte, ca., LATP/PVDF-TrFE/ILE, composing of ceramic LATP, PVDF-TrFE polymer, and a small amount of high Li concentration ILE ($0.4LiFSI$ (lithium bis(fluoromethanesulfonyl) imide)-$0.6Pyr_{14}FSI$), among which the PVDF-TrFE polymer connects LATP particles via forming 3D networks to enable the preparation of thin and flexible films, while the highly concentrated ILE facilitates the electrode|electrolyte interfacial contact, improves the overall ionic conductivity, and reinforce the interfacial electrochemical stability against Li.

Nevertheless, due to the thermodynamically unstable interface between LATP and lithium, the single protection of highly concentrated ILE is not sufficient. Herein we report a thin layer of poly[2,3-bis(2,2,6,6-tetramethylpiperidine-N-oxycarbonyl)-norbornene] (PTNB) coated on lithium metal via a facile dip-coating method, together with the high Li concentration ILE ($0.4LiFSI-0.6Pyr_{14}FSI$), acting as the protection interlayer between lithium and LATP. Fortunately, the additional thin PTNB polymer coating layer on lithium metal (PTNB@Li) guarantees a further isolation of the direct contact between LATP and lithium metal. Additionally, PTNB, which manifests poor electrical conductivity, is capable of facilitating the uniform distribution of Li$^+$ flux and thus suppressing the lithium dendrites generation.[17,47,48] PTNB between lithium metal and hybrid electrolyte possess a fast self-exchange reaction of the nitroxide radical to transfer lithium cation to lithium metal or hybrid electrolyte.[49–51] Without the PTNB coating

**ADVANCED
SCIENCE NEWS**
www.advancedsciencenews.com

**ADVANCED
ENERGY
MATERIALS**
www.advenergymat.de

layer, the lithium stripping-plating lifetime is ended after 128 h, fortunately, the implementation of PTNB@Li extends the lithium stripping-plating lifetime to ≈800 h, concomitantly with no lithium dendrites formed. When evaluating PTNB@ Li‖LiNi$_{0.8}$Co$_{0.1}$Mn$_{0.1}$O$_2$ (PTNB@Li‖NCM$_{811}$) cells, the drastically decreased interfacial resistances, prohibited dendritic lithium generation, better-preserved cathode material structure with barely any microcracks, and thinner interphase formation for both PTNB@Li and NCM$_{811}$ lead to an upgraded rate capability as well as cycling stability. Notably, the PTNB@Li‖NCM$_{811}$ cells function impressively over a wide temperature range (from −10 °C) exhibiting very stable cyclability even at 0 °C. PTNB@ Li‖NCM$_{811}$ prototype cells operate efficiently via powering the LED light when rolled into a cylindrical shape and cut into a few pieces (Video S1, Supporting Information), highlighting the inherently high safety profile. Even though a small amount of ILE was introduced as a "proof-of-concept" study, the quasi-solid-state lithium metal cells enable the fabrication of multi-layer bipolar cells.

2. Results and Discussion

2.1. Material Characterizations

As evident in Figure S1a,S1b, Supporting Information, the majority of LATP particles display round-shape morphology with a particle size around 1–2 μm. The X-ray diffraction (XRD) pattern of LATP powder (Figure S1c, Supporting Information) reveals that all the characteristic peaks are in accordance with the rhombohedral NASICON-type LiTi$_2$(PO$_4$)$_3$ phase.[30] The sharp, high-intensity diffraction peaks indicate the high crystallinity of the LATP powder, which is maintained also after the 20 min wetting in DIW during the LATP/PVDF-TrFE film production (Figure S1c, Supporting Information).

Figure 1a–d shows scanning electron microscopy (SEM) images of the LATP/PVDF-TrFE film. The image obtained at low magnification (Figure 1a) shows a quite uniform, compact, and dense film without any cracks. The thickness of the LATP/ PVDF-TrFE film is about 90 μm (Figure 1c). From Figure 1b (top-view) and Figure 1d (cross-section view), we see that the LATP particles are well-connected by PVDF-TrFE polymer networks, which are expected to provide sufficient flexibility. This is verified by the optical images as illustrated in Figure 1e,1f, where a free-standing and flexible "paper-like" thin film (about 10 cm × 13 cm) is displayed. Figure S1d, S1e and Figure S1f, S1g, Supporting Information, show, respectively, the top and cross-sectional images of LATP/PVDF-TrFE/ILE hybrid film, that is, after impregnation with ILE. Notably, ILE is well infiltrated into the pores of LATP/PVDF-TrFE film. Finally, Figure S1h,S1i, Supporting Information, present optical photos of LATP/PVDF-TrFE/ILE hybrid film.

For the thermal stability evaluation of the as-obtained LATP/ PVDF-TrFE/ILE hybrid film, the thermogravimetric analysis (TGA) measurement was performed (Figure 1g). As expected, the LATP powder shows high thermal stability with no weight loss upon heating up to 700 °C. The LATP/PVDF-TrFE film is thermally stable up to 352 °C, and the weight loss is estimated
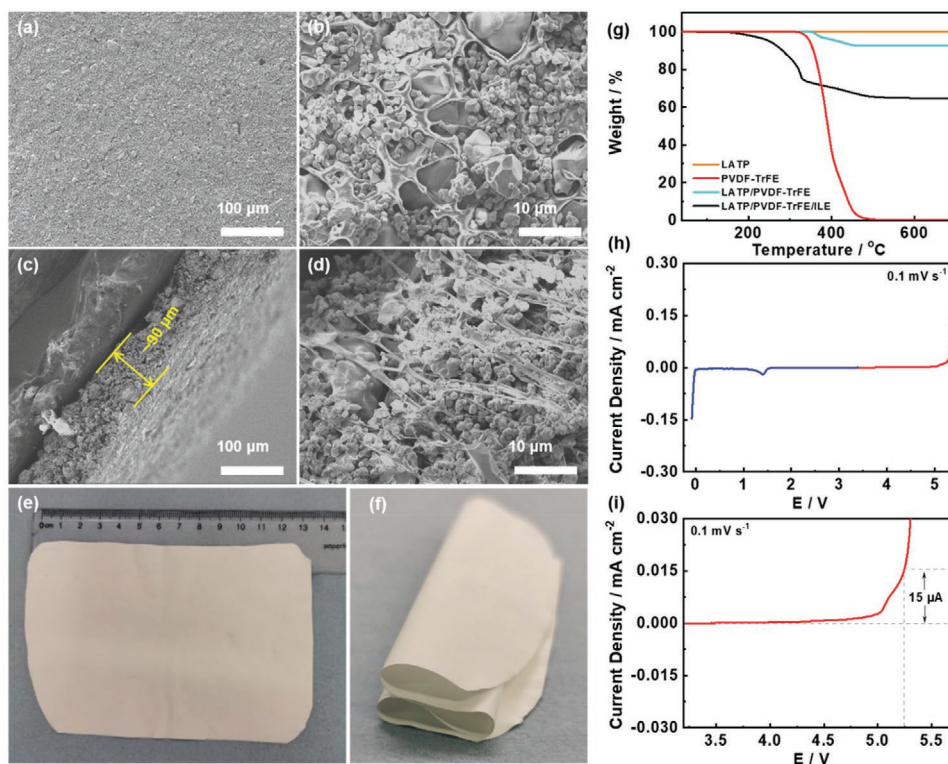
Figure 1. a,b) Top view and c,d) cross-section view of the LATP/PVDF-TrFE film; e,f) optical images of a piece of LATP/PVDF-TrFE film (≈10 × 13 cm^2); g) TGA profiles of LATP powder (yellow), PVDF-TrFE polymer (red), LATP/PVDF-TrFE film (turquoise), and LATP/PVDF-TrFE/ILE hybrid film (black); h,i) ESW of the LATP/PVDF-TrFE/ILE hybrid film.

to be ≈8 wt% showing a good agreement with the input ratio, implying that the PVDF-TrFE polymer is homogeneously distributed within the hybrid film. The TGA profile of LATP/PVDF-TrFE/ILE hybrid film can be divided into two regions. Below 328 °C, the weight loss is mostly attributed to the decomposition of ILE, suggesting that it accounts for approximately 24.4 wt% of the total weight. Between 328 and 522 °C, the weight loss is dominated by PVDF-TrFE polymer. The addition of ILE reduces the overall thermal stability, nevertheless, the hybrid film is still thermally stable up to 180 °C (the onset temperature is defined by 1 wt% of weight loss).

Given the presence of ILE and PVDF-TrFE polymer, it is necessary to conduct the flammability test of our quasi-solid hybrid electrolyte film. A piece of LATP/PVDF-TrFE/ILE hybrid film (Video S2, Supporting Information) and a piece of glass fiber separator (GF-A) soaked with liquid electrolyte (LP30, Video S3, Supporting Information) were exposed to a direct flame. The ignition of glass fiber triggered the continuous burning in conjunction with the release of heavy smokes, whereas no flames or smokes were observed when burning the LATP/PVDF-TrFE/ILE hybrid film indicating its "self-extinguishing" feature.

The electrochemical stability of LATP/PVDF-TrFE/ILE hybrid film was determined by electrochemical stability window (ESW) composing of two linear sweep voltammetry (LSV) scans (anodic and cathodic, Figure 1h). The weak peak located at about 1.4 V can be assigned to the initial SEI formation[52,53] as well as the contribution from an impurity present in LiFSI. As a matter of fact, the same peak appears in the cathodic scans of ILEs with different LiFSI content (Figure S2, Supporting Information), that is, from $0.5LiFSI-0.5Pyr_{14}FSI$ to $0.4LiFSI-0.6Pyr_{14}FSI$ and to $0.3LiFSI-0.7Pyr_{14}FSI$, but decreases with the LiFSI content. The oxidation stability is revealed to be >5.2 V as seen from the magnified anodic scan profile (Figure 1i) when defining the maximum acceptable current density flow to be 15 µA cm^{-2}. Such high oxidation stability implies good compatibility with high voltage cathodes, that is, nickel-rich NCM. It is worth mentioning that the ESW of PTNB is also rather large (Figure S3, Supporting Information), that is, >5.5 V.

The ionic conductivity of pure ILE is determined to be 1.18 mS cm^{-1} (Figure S4a, Supporting Information), higher than that of the LATP/PVDF-TrFE/ILE hybrid electrolyte (0.31 mS cm^{-1}, Figure S4b, Supporting Information).

2.2. Impact of PTNB Coating Layer on Compatibility of LATP/PVDF-TrFE/ILE Hybrid Electrolyte With Li

To find out the appropriate PTNB coating amount, the concentration of PTNB dissolved in DME was tuned, ca., 0.4, 1, and 2 wt%. Prior to any surface treatment, the morphology of a fresh Li foil was first examined by SEM, as demonstrated in Figure S5a,S5b, Supporting Information. The fresh Li exhibits a fairly clean and smooth surface. The line traces are due to the extrusion during fabrication, while the tiny white dots correspond to the presence of Li_2CO_3 (Figure S6, Supporting Information) that can potentially form during the fabrication, storage, as well as the sample preparation steps. All the samples were, in fact, prepared in the dry room (dew point - 60 °C at 20 °C), where only the humidity was controlled; with the Li 1s spectrum

showing no presence of LiOH. After coating with PTNB, the surface of PTNB@Li becomes rougher when increasing the PTNB concentration (Figure S5c, S5e,S5g, Supporting Information). Focusing on the images taken at higher magnification, the coating layer made with the 0.4 wt% PTNB solution appears to be rather thin as the features present on the pristine Li foil are still visible (Figure S5d, Supporting Information). The coating obtained with the 1 wt% PTNB solution coated Li displays a thicker but more homogenous coating layer (Figure S5f, Supporting Information). Whereas, the coating layer made with the 2 wt% PTNB solution presents severe cracks (Figure S5h, Supporting Information), which makes it not suitable for further study.

Lithium stripping-plating tests were carried out to investigate the interfacial compatibility between lithium metal and LATP/PVDF-TrFE/ILE hybrid electrolytes. Without the highly concentrated ILE, the overpotential of Li|LATP/PVDF-TrFE|Li symmetric cell quickly exceeds 2 V after a 6 h aging step (results not shown), indicating huge interfacial resistance due to the spontaneous reaction between LATP and lithium metal as well as the poor physical interfacial contact. Therefore, this sample is excluded from the following studies. The addition of ILE to the electrolyte, ca., Li|LATP/PVDF-TrFE/ILE|Li (denoted as Li‖Li hereafter), substantially reduces the overpotential to 34 mV (3rd cycle, red curve in **Figure 2a**) at a current density of 0.1 mA cm^{-2}, predominantly attributed to the improved interfacial contact and enhanced electrode wettability. Furthermore, this enables a stable cycling for 94 h. Afterward, the overpotential gradually decreases till 128 h when the cell's stripping-plating voltage profile takes the perfect rectangular shape typical of a short circuit (left inset in Figure 2a). This means that the highly concentrated ILE interlayer is capable of mitigating the side reactions between LATP and lithium metal, but, only to a certain extent. With the additional PTNB protection interlayer, the cycling lifetime of PTNB@Li|LATP/PVDF-TrFE/ILE|PTNB@Li (denoted as PTNB@Li‖PTNB@Li) cell is further prolonged. Unlike the gradually increasing overpotential evidenced by the Li‖Li cell (after the initial sharp overpotential drop), the PTNB@Li‖PTNB@Li cells present a trend of gradually decreasing overpotential primarily due to the reorganization of the lithium metal|electrolyte interface resulting in the surface chemistry changing from the native layer (always present on Li metal) to the SEI. With the thinner coating (0.4 wt% PTNB), the lifetime of the PTNB@Li‖PTNB@Li_0.4 wt% cell is prolonged to 182 h (blue curve in Figure 2a) prior to the typical fingerprint of a short-circuited cell appears. A higher decreasing rate of overpotential is observed after about 600 h in the case of PTNB@Li‖PTNB@Li_1 wt% cell, which is presumably due to the formation of "soft short-circuit", nevertheless, a greatly prolonged cycling lifetime, that is, more than 792 h (black curve in Figure 2a) is achieved, indicating that the coating layer obtained using the 1 wt% PTNB solution can effectively and substantially suppress dendritic lithium formation. What's more, even after 792 h of cycling, no sign of cell circuit is evidenced (right inset in Figure 2a). Owing to the presence of a polymer coating layer at each Li electrode, the overpotential of PTNB@Li‖PTNB@Li_1 wt% cell is slightly larger than that of Li‖Li cell, that is, 36 versus 34 mV (3rd cycle). Nevertheless, a lower overpotential of the PTNB@Li‖PTNB@Li_1 wt% cell is observed after 24 h,
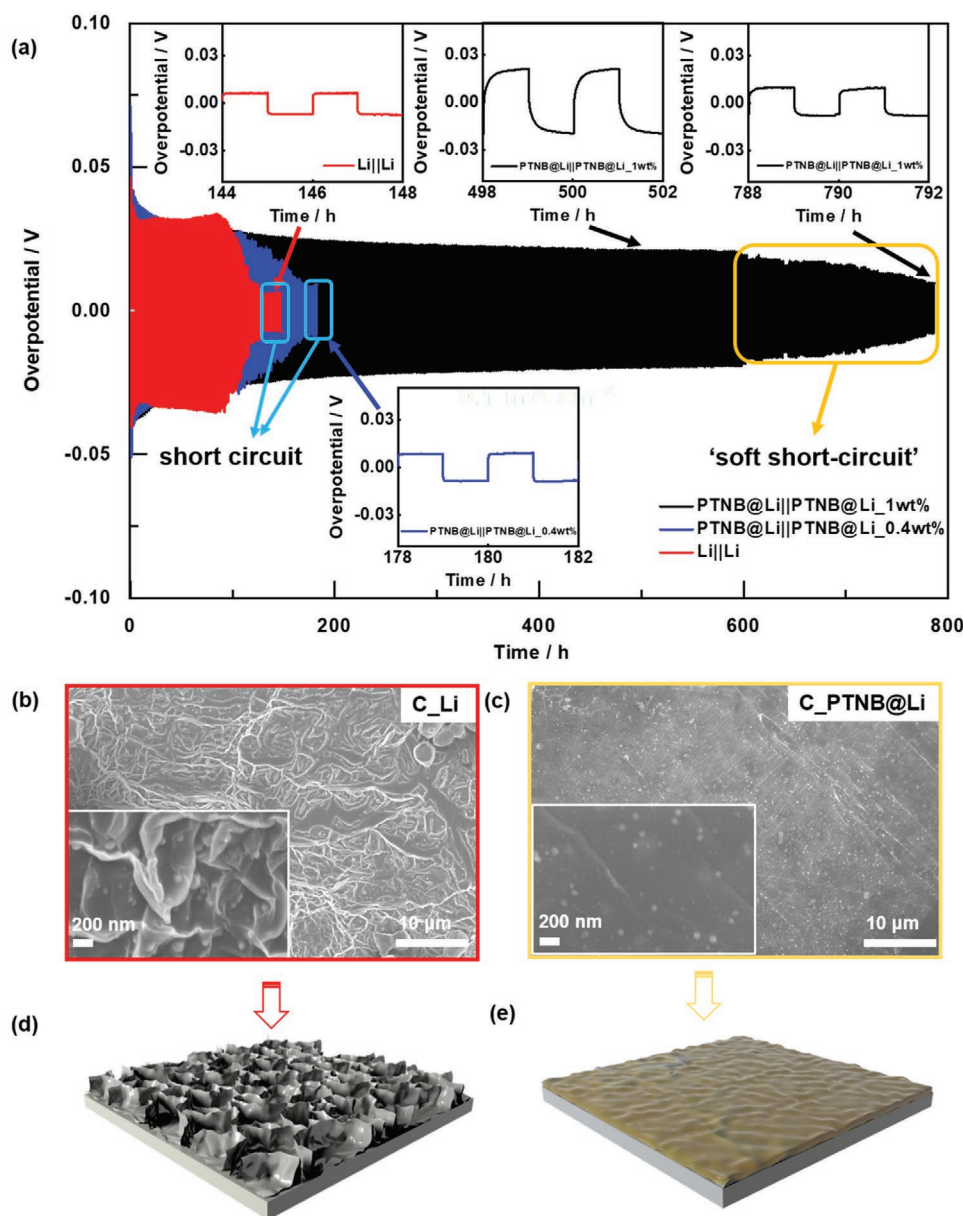
Figure 2. a) Comparative lithium stripping-plating profiles of Li||Li, PTNB@Li||PTNB@Li_0.4 wt%, and PTNB@Li||PTNB@Li_1 wt% cells; ex situ morphology investigation of recovered b,d) C_Li and c,e) C_PTNB@Li electrodes from Li||Li, and PTNB@Li||PTNB@Li_1 wt% cells.

compared to the Li||Li cell. Given the fact that 1 wt% PTNB coated Li shows prolonged stability, it was selected for the following studies.

To determine the reason behind such a different lithium stripping-plating behavior, both symmetric cells were disassembled and the lithium morphology was examined by post mortem SEM analysis. Taking a glance at the SEM images obtained at a low magnification (Figure S7a,S7b, Supporting Information), it is evident that plenty of LATP agglomerates accumulate on the surface of the cycled lithium electrode (C_Li) even after rinsing, implying that relatively strong adhesion exists between these LATP particles and lithium metal. In sharp contrast, the surface of the cycled PTNB@Li electrode

(C_PTNB@Li) is much cleaner and flatter. Increasing the magnification, notably, the C_Li shows highly pleated morphology with enormous "flake-like" lithium dendrites (Figure 2b, 2d). In sharp contrast, the C_PTNB@Li has a well-preserved surface with slightly bumpy morphology (Figure 2c,2e). The comparative investigation on ex situ morphology confirms that the PTNB coating layer can effectively suppress the dendritic lithium formation and further proliferation. It was reported that the nitroxide radical in PTNB, which exhibits a high ionic conductivity of 7.05 mS cm^{-1} at 25 °C (Figure S8, Supporting Information), favors the fast charge transfer of lithium cation via an n-type reaction.[49–51] Thus, lithium cations are homogeneously transferred to neighboring monomers that contain the

ADVANCED
SCIENCE NEWS
www.advancedsciencenews.com

ADVANCED
ENERGY
MATERIALS
www.advenergymat.de

nitroxide radical during a fast self-exchange reaction. Therefore, the coated PTNB not only prevents the growth of lithium dendrites but also improves the electrochemical reaction with fast lithium-ion transfer to lithium metal or hybrid electrolyte.

2.3. Impact of PTNB Coating Layer on Galvanostatic Cycling and Rate Capability

For the evaluation of electrochemical performance of lithium metal, as such or coated with the PTNB interlayer as the negative electrode, the rate performance of cells incorporating NCM_{811} as the positive electrode and LATP/PVDF-TrFE/ILE as the electrolyte, was first investigated (**Figure 3**a–c). Compared to the Li‖NCM_{811} cell, the PTNB@Li‖NCM_{811} cell

delivers considerably higher overall capacities at all C-rates, to name a few, 197.7 versus 179.7 mAh g^{-1} (0.05C), 194.7 versus 170.0 mAh g^{-1} (0.1C), 185.5 versus 155.1 mAh g^{-1} (0.2C), 171.3 versus 119.3 mAh g^{-1} (0.5C), 154.4 versus 44.7 mAh g^{-1} (1C), and 123.0 versus 23.9 mAh g^{-1} (2C), respectively. A more direct and detailed comparison of the capacity delivered at the various current densities is provided in Table S1, Supporting Information. The substantially lower capacity at a low C-rate (0.05C) of the Li‖NCM_{811} cell reflects the poor chemical stability of LATP hybrid electrolyte against lithium metal, resulting in a large interfacial resistance. At higher C-rates, the capacity decay is even more pronounced due to poor electronic/ionic kinetics. Also, the initial Coulombic efficiency (ICE) of the Li‖NCM_{811} cell is considerably lower than that of the PTNB@Li‖NCM_{811} cell (82.8% vs 87.9%, see Figure 3b,3c), suggesting
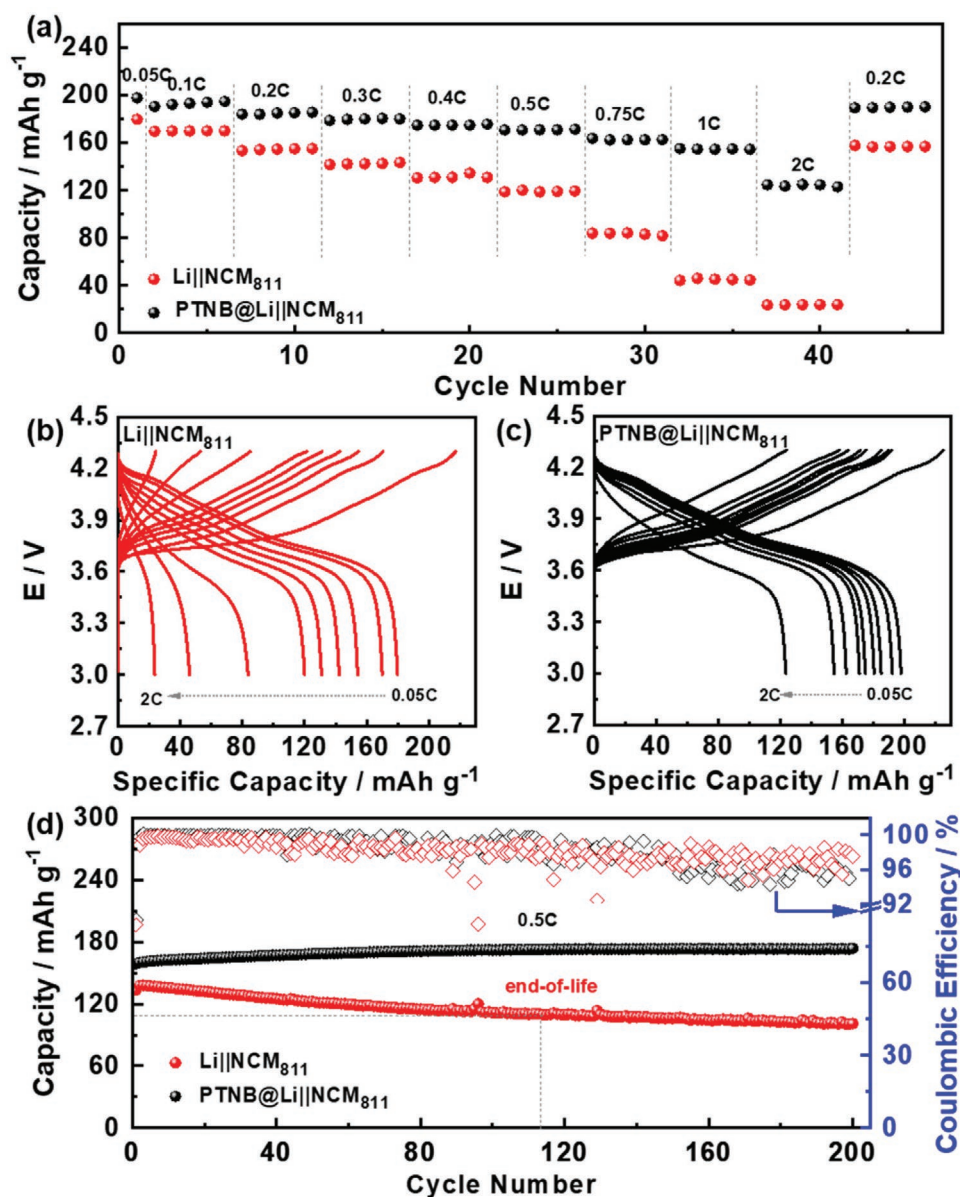
Figure 3. Comparative a–c) rate capability and d) long-term cycling stability among the Li‖NCM_{811} (red) and PTNB@Li‖NCM_{811} (black) cells (T = 20 °C).

a larger irreversible capacity loss due to stronger initial side reactions. When reverting to the same current density (0.2C), the PTNB@Li‖NCM$_{811}$ cell actually delivers a higher capacity (190.1 vs 185.5 mAh g^{-1}), which could be due to the slower activation process. On the contrary, The Li‖NCM$_{811}$ cell retains only 98.9% of the initial capacity. The capacity delivered by PTNB@ Li‖NCM$_{811}$ cell is comparable to that achieved with carbonate-based liquid electrolyte system (1 M LiPF$_6$ in EC:DEC (1:1 wt) with 1 wt% of VC, that is, 206.9 mAh g^{-1} (0.1C, Figure S9, Supporting Information).

Next, the long-term cycling stability was studied by subjecting fresh cells to 200 cycles at 0.5C after the formation cycles (Figure 3d). The Li‖NCM$_{811}$ cell delivers an initial capacity of 133.6 mAh g^{-1}. A few cycles later, the capacity reached 138.0 mAh g^{-1}, but followed by continuous capacity degradation to 101.0 mAh g^{-1} after 200 cycles, leading to a capacity retention ratio of 73.2%. The end-of-life criterion (80% of initial capacity retention) is already met after 112 cycles. With the protected PTNB@Li electrode, however, a much higher initial capacity (158.7 mAh g^{-1}) is delivered. Upon cycling, the capacity delivered by the PTNB@Li‖NCM$_{811}$ cell increases, reaching, after approximately 110 cycles, 173.6 mAh g^{-1}. This increase is most likely due to the slow wetting of the highly concentrated ILE, which has rather high viscosity. After approximately 100 cycles, however, the Coulombic efficiency (CE) of the PTNB@Li‖NCM$_{811}$ cell decreases to somehow random values between 95 and 99%. A possible explanation for this behavior is the formation of small dendrites leading to charge extra capacity, which, however, strongly depends on the surface of the used lithium foil (see later in text and Figure 7). Overall, the PTNB coating undoubtedly plays a critical role in substantially upgrading the cycling stability as well as the deliverable capacities.

2.4. Mechanism Investigations on the Enhanced Performance Enabled by PTNB Coating

In order to understand the role of PTNB coating for boosting electrochemical performance, we first completed the electrochemical impedance spectroscopy (EIS) measurements at both charge (4.3 V) and discharge (3.0 V) states upon cycling to comparatively study the evolutions of electrode kinetics of Li‖NCM$_{811}$ and PTNB@Li‖NCM$_{811}$ cells. It is known that lithiated NCM$_{811}$ generally exhibits nearly negligible charge-transfer resistance compared to the lithium metal side.[54] As a result, at discharge status, the depressed semicircle at high-frequency range can be mainly assigned to the electrical contact resistance between Al current collector and NCM$_{811}$ composite, and the interfacial resistance of Li and LATP/PVDF-TrFE/ILE hybrid electrolyte.[55,56] The former tends to remain constant at various state-of-charge (SOC) unless noticeable volume change occurs upon de-/lithiation. At open-circuit voltage (OCV) state, these two cells show similar overall resistances. However, the depressed semicircle of Li‖NCM$_{811}$ (**Figure 4a**) grows substantially upon cycling, implying a vast accumulation of interfacial resistance between Li and the hybrid electrolyte mainly due to unavoidable detrimental side reactions. In the delithiated state (Figure 4b), given the fact that the resistance from the NCM$_{811}$‖hybrid electrolyte interface is no longer negligible,

we approximately assign the resistance contribution between the turning point at lithiated state, that is, 54.9 Hz (Figure 4a) and the turning point at delithiated state, that is, 2.6 Hz to the interfacial resistance of NCM$_{811}$‖hybrid electrolyte. The overall interfacial resistances of Li‖hybrid electrolyte interface at delithiated state are elevated in contrast to those at lithiated state. A possible reason is the formation of thicker SEI at a higher SOC state.[57] Upon cycling, an impedance increase including the charge-transfer as well as the cathode electrolyte interphase (CEI) resistance is also observed with respect to the NCM$_{811}$‖hybrid electrolyte interface. Hence, the huge and continuously growing resistances at both Li‖hybrid electrolyte and NCM$_{811}$‖hybrid electrolyte interfaces explain the low deliverable capacity and strong capacity decay evidenced in Li‖NCM$_{811}$ cell (Figure 3d).

With the additional protective PTNB interlayer (Figure 4c, 4d), the overall resistances at both de-/lithiated states are dramatically reduced by at least one order of magnitude. Considering that the majority of the resistance comes from lithium metal, it is plausible that such a drastic improvement is (predominantly) due to the effective protection of Li‖hybrid electrolyte interface. Nevertheless, a mild increase of the interfacial resistance at the lithium electrode is still evidenced upon cycling (Figure 4c), which is possibly caused by increasing decomposition products accumulating on the lithium surface. Unlike the Li‖NCM$_{811}$ cell, the Li‖hybrid electrolyte interfacial resistance in PTNB@Li‖NCM$_{811}$ cell remains more or less unchanged at different SOCs (i.e., 3.0 and 4.3 V), suggesting very thin and stable SEI formation during de-/lithiation. The resistance from NCM$_{811}$‖hybrid electrolyte interface is constant over 200 cycles, revealing a very stable NCM$_{811}$‖hybrid electrolyte interface in PTNB@Li‖NCM$_{811}$ cell. The quite stable interface at the lithium metal side and very stable interface at the NCM$_{811}$ side agree very well with the markedly enhanced electrochemical performance shown in Figure 3d. Subsequently, these cells were disassembled for post mortem analysis. The optical images (Figure S10a,S10b, Supporting Information) show a distinct difference in the cycled LATP/PVDF-TrFE/ILE hybrid films. Without the protection of PTNB coating layer, the LATP/PVDF-TrFE/ILE hybrid film face in contact with lithium metal appears black, indicating severe interfacial side reactions between LATP and Li. On the other hand, such a phenomenon is significantly suppressed with the protection of PTNB. Through comparing the cross-section view of the interface of LATP/PVDF-TrFE/ILE and Li (Figure S10c, S10d, Supporting Information), we observe a considerably reduced thickness (≈94 μm) of lithium metal in the cycled Li‖NCM$_{811}$ cell, which is nearly 60 μm higher than that of the cycled PTNB@Li‖NCM$_{811}$ cell. Meanwhile, the higher thickness of LATP/PVDF-TrFE/ILE is evidenced in the cycled Li‖NCM$_{811}$ cell, that is, ≈198 versus 149 μm (PTNB@ Li‖NCM$_{811}$ cell). These results verify that PTNB successfully suppresses the detrimental reactions between LATP and Li leading to a substantially reduced consumption of Li and electrolyte volume expansion consistently with the EIS results (Figure 4).

The substantially higher interfacial resistance of Li‖hybrid electrolyte with respect to that of the PTNB@Li‖hybrid electrolyte led us to investigate the interphases forming in the two cases. Ex situ XPS measurements were performed to analyze
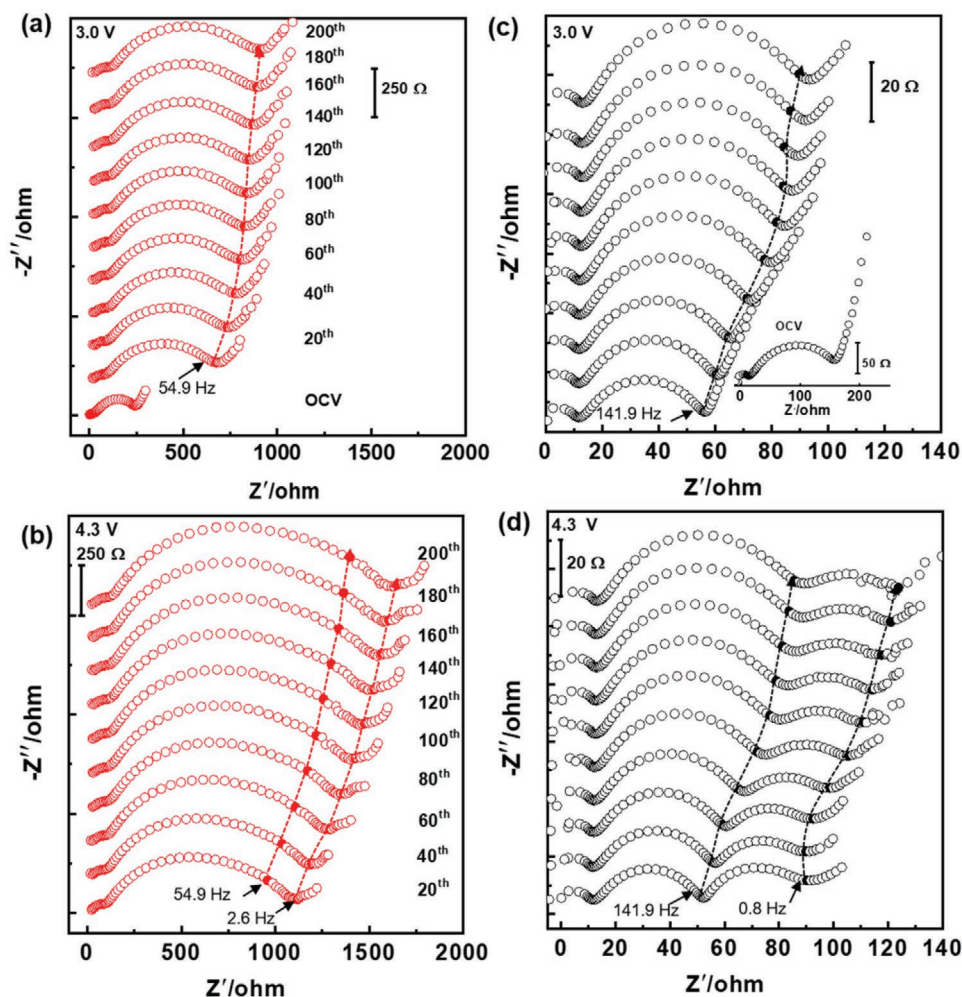
Figure 4. The Nyquist plots of Li‖NCM$_{811}$ cell measured at a) 3.0 and b) 4.3 V. The Nyquist plots of PTNB@Li‖NCM$_{811}$ cell measured at c) 3.0 and d) 4.3 V.

the surface as well as the depth profiling (5 min and 10 min of ion bombardment) of cycled Li and PTNB@Li recovered from Li‖NCM$_{811}$ and PTNB@Li‖NCM$_{811}$ cells. The interphase of Li is mainly composed by Li$_2$CO$_3$ (≈532 eV) at all studied depth profiles, as is observed in the O 1s spectrum (**Figure 5a**).[58] The presence of a high amount of Li$_2$CO$_3$ corresponds mainly to the native SEI of the fresh Li (see Figure S6, Supporting Information). Additionally, Li$_2$O (528.6 eV) and species with -SO- bonds (532.2 eV) are observed.[59–61] The former is already presented in the native SEI (Figure S6, Supporting Information) of fresh Li and the latter corresponds to the FSI$^-$ anion and its decomposition products. On the other hand, the O 1s surface spectrum of cycled PTNB@Li (Figure 5b), shows two extra peaks with respect to Li, which correspond to the PTNB coating layer, −C−N−O at 530.2 eV—also observed in N 1s photoemission line (Figure S11, Supporting Information), and − (C=O)−O−CR at 533.9 eV.[58,61,62] This indicates that PTNB still exists even after 200 cycles and that the formed interphase is thin, although the peaks corresponding to the PTNB disappear after 5 min Ar$^+$ sputtering, showing a similar interphase as in Li at higher depths, formed by Li$_2$CO$_3$ and -SO- bond species from the ILE salt and its decomposition product.

The main difference in the formed interphase between Li and PTNB@Li is observed in F 1s photoemission line. The comparison of F 1s in Figure 5a and Figure 5b reveals that a much higher amount of LiF (at 685 eV)[62] is formed on the surface of cycled Li comparing to that of the PTNB@Li. The presence of fluorine corresponds to the FSI$^-$ anion of the ILE, hence the FSI$^-$ is reduced to LiF to a greater extent in the Li‖NCM$_{811}$ cell than in the PTNB@Li‖NCM$_{811}$ one. The high resistivity feature of LiF is in line with the substantially higher interfacial resistance between Li and hybrid electrolyte observed from the EIS result (Figure 4a, 4b).

In order to understand the FSI$^-$ anion decomposition products, S 2p photoemission lines of cycled Li and PTNB@Li were collected and the deconvolution of the peaks are illustrated in Figure 5a and Figure 5b, respectively. Both systems show the same species on the surface, including the "pure" FO$_2$SN$^-$SO$_2$F at 169.5 eV and the reduced $^-$N-SO$_2$F at ≈168.5 eV.[63,64] The former one can be assigned to the remaining FSI$^-$ anion (probably as LiFSI salt) and the latter to the reduced product of LiFSI. Notably, the peak intensity for both contributions is considerably higher in the cycled Li than in the cycled PTNB@Li. This implies that the Li interphase is composed of a higher amount of LiFSI and reduced LiFSI than the formed interphase

ADVANCED
SCIENCE NEWS
www.advancedsciencenews.com

ADVANCED
ENERGY
MATERIALS
www.advenergymat.de
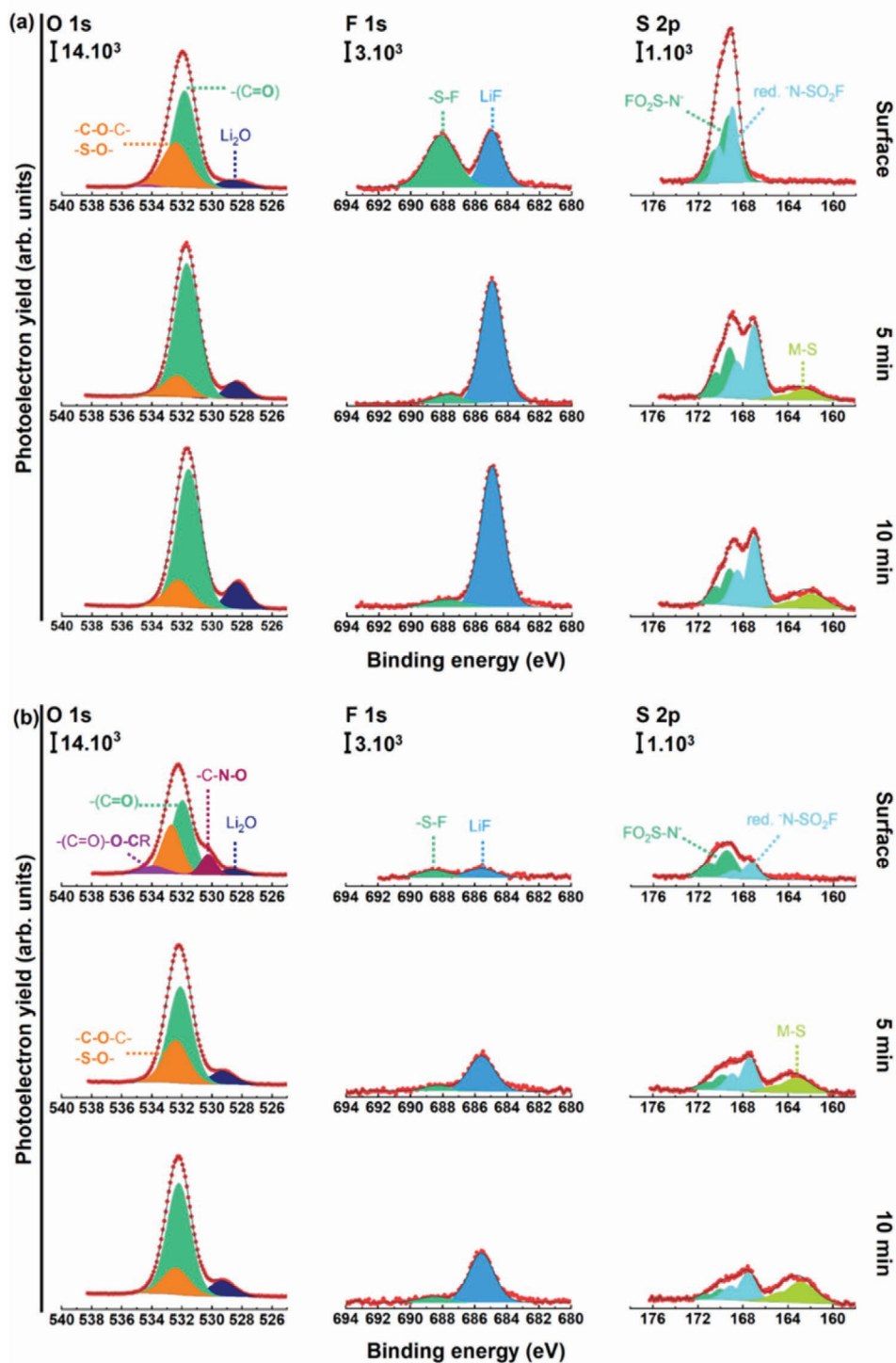
Figure 5. O 1s, F 1s, and S 2p photoelectron lines at different depths (surface and after 5 and 10 min Ar$^+$ sputtering) of cycled a) Li metal and b) PTNB@ Li recovered from Li‖NCM$_{811}$ and PTNB@Li‖NCM$_{811}$ cells respectively.

on PTNB@Li; in agreement with the F 1s spectra. Indeed, the higher reduced salt product together with the substantially higher LiF in cycled Li surface infer that the formed interphase is much thicker due to more severe side reactions at the interface between bare Li and hybrid electrolyte. Besides, the higher remaining salt at higher depth (5 and 10 min) in cycled Li is presumably due to the thicker and denser interphase, which traps more salt. The ex situ XPS analysis affirms that the PTNB coating layer is very effective in reducing side reactions and forming thinner interphase at the lithium metal side.

We also explored the possible impact of PTNB on the positive electrode side. The ex situ morphology examinations of NCM_{811} cathodes, was implemented by SEM. **Figure 6a**,6b and Figure 6d, 6e present the surface morphology of a cycled NCM_{811} particle recovered from Li‖NCM_{811} and PTNB@ Li‖NCM_{811} cells, respectively. Taking a first glance at the SEM images (Figure 6a, 6d) measured at low magnification, it seems that both particles are quite intact. Although, when increasing magnifications, without the protection of PTNB coating layer at the lithium metal side, the primary particles of NCM_{811} undergo severe damage and exhibit a rougher surface (Figure 6b). This means that the detrimental side reactions occur not only at the lithium metal side but also at the NCM_{811} side. On the contrary, the surface of the NCM_{811} particle recovered from PTNB@ Li‖NCM_{811} cell remains quite clean and well-preserved. This is further corroborated by ex situ XPS analysis of cycled NCM_{811} electrodes, as demonstrated by O 1s in Figure S12, Supporting

Information. The M-O peak corresponds to the metal (Ni, Co, and Mn) oxygen bonding of the NCM_{811}. Comparing the ratio between the M−O with the O−C and O−S containing contributions (−(C=O), −C−O−C−, −S−O−, and −(C=O)−O−CR)− noting that these peaks are related with the electrolyte decomposition reaction products, this means that the thinner CEI layer is formed on the surface of NCM_{811} recovered from PTNB@Li‖NCM_{811} cell.

Shifting our focus from surface to bulk, the bulk morphology was subsequently examined with the aid of a focused ion beam (FIB). For each specimen, we cut 7–8 secondary particles. A representative particle of each sample is shown in Figure 6c and Figure 6f, respectively. Within the NCM_{811} secondary particle (Li‖NCM_{811}, Figure 6c), plenty of cracks propagating from the inner core to outer surface regions are evidenced and agree with the increased NCM_{811}|hybrid electrolyte interfacial impedance contribution upon cycling. In contrast, the NCM_{811} sample
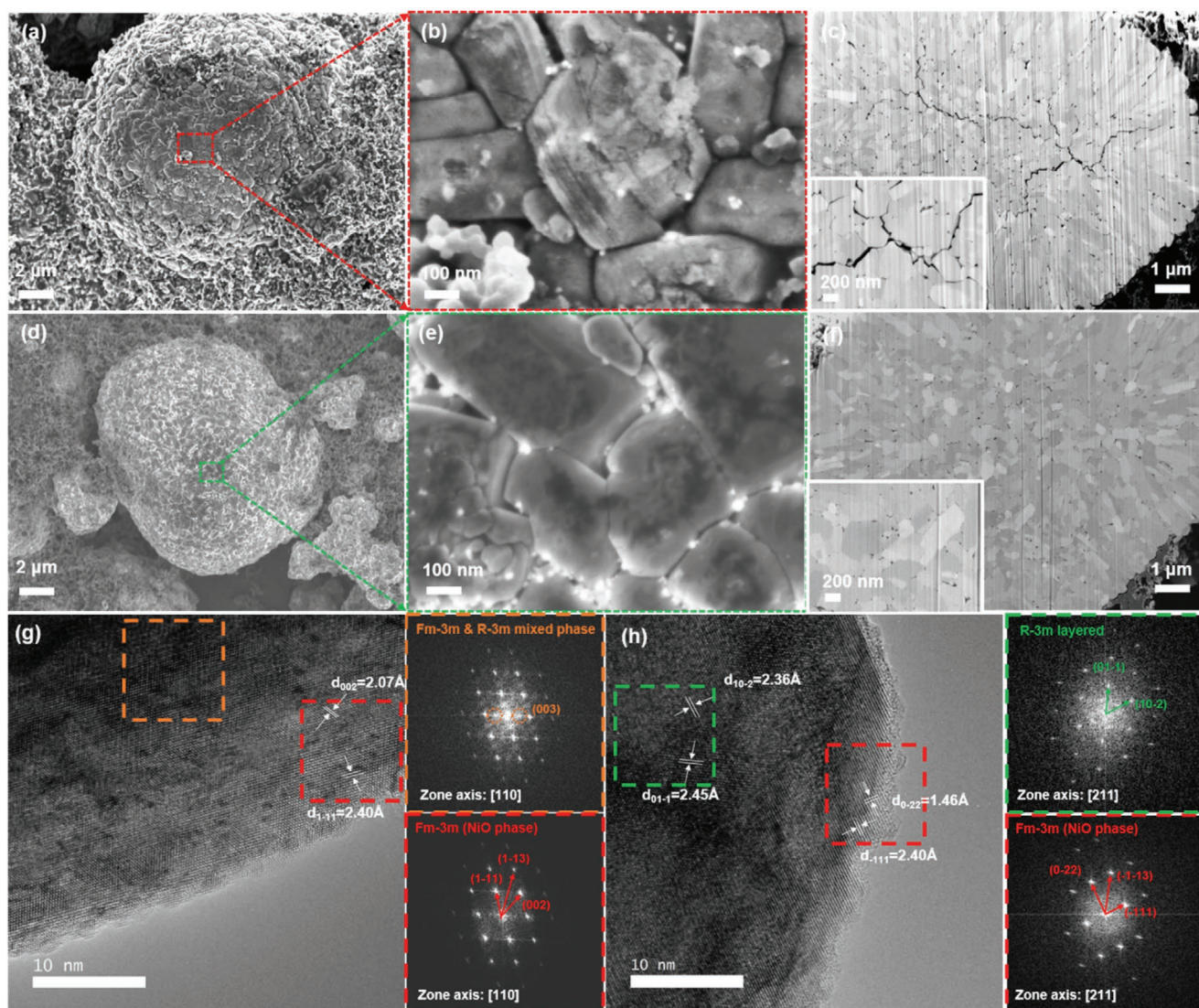
Figure 6. Ex situ a,b) surface and c) cross-sectional SEM images of cycled NCM_{811} particles recovered from Li‖NCM_{811} cells. Ex situ d,e) surface and f) cross-sectional SEM images of cycled NCM_{811} particles recovered from PTNB@Li‖NCM_{811} cells. Ex situ high-resolution TEM images and corresponding FFT patterns of NCM_{811} particles recovered from g) Li‖NCM_{811} and h) PTNB@Li‖NCM_{811} cells.

ADVANCED
SCIENCE NEWS
www.advancedsciencenews.com

ADVANCED
ENERGY
MATERIALS
www.advenergymat.de

(PTNB@Li‖NCM$_{811}$, Figure 6f) exhibits no obvious micro-cracks, suggesting that the harmful parasitic reactions at the positive electrode side are substantially suppressed thanks to the protection of PTNB at the lithium metal side.

It has been reported that the anisotropic lattice contraction upon cycling is predominantly responsible for the structural degradation of LiNi$_x$Co$_y$Mn$_{1-x-y}$O$_2$ (with x > 0.8).[65,66] As a consequence, the mechanical stress induced by phase changes triggers the propagation of internal microcracks to the particle surface.[67] The distinctive behavior regarding the formation of microcracks demonstrated in Figure 6c and Figure 6f leads us to subsequently investigate the structure of cycled NCM$_{811}$ particles. Figure 6g and Figure 6h display the high-resolution transmission electron microscope (HRTEM) images of both cycled NCM$_{811}$ samples recovered from Li‖NCM$_{811}$ and PTNB@Li‖NCM$_{811}$ cells respectively. As anticipated from the bulk analysis (Figure 6c), at the outmost surface, the remarked region (red dash box, Figure 6g) and its corresponding fast Fourier transform (FFT) pattern reveal a structure change from the original layered (R-$3m$) structure to a NiO-like rock-salt (Fm-$3m$) structure.[4,65] The relatively inner region marked in an orange dash box and its corresponding FFT pattern reveal a mixed phase of layered and rock salt structure. Nevertheless, the weak (003) diffraction (marked in a dash orange circle) that can be assigned to the layered structure along the (111) diffraction direction of the rock-salt structure indicates that the rock-salt structure still dominates in the inner region. This implies that the outer surface undergoes stronger structural degradation predominantly caused by detrimental parasitic reactions between the electrode and electrolyte at highly delithiated status.[37,68,69] Similarly, the rock-salt phase marked in the red dash box (Figure 6h) is also found at the outmost surface of NCM$_{811}$ recovered from PTNB@Li‖NCM$_{811}$ cell. Nonetheless, with a protecting layer of PTNB at the lithium metal side, the inner part of the NCM$_{811}$ remains in the layered structure (green dash box and its corresponding FFT pattern), signifying that the undesired structural degradation is significantly mitigated.

The above ex situ SEM, XPS, and TEM analyses detail that the surface, as well as the bulk stability of NCM$_{811}$, can be improved to a large extent by the presence of a PTNB coating layer on the lithium metal surface. The inferior performance of NCM$_{811}$ coupled with bare Li can be explained by the uneven Li$^+$ flux at lithium metal surface, which can induce the formation of lithium dendrites and trigger the potential fluctuations at the NCM$_{811}$ side whilst leading to harsh conditions (i.e., over-charge, over-discharge) for the operation of NCM$_{811}$. In line with the EIS results (Figure 4), the degradations of both Li metal and NCM$_{811}$ cathode material within Li‖NCM$_{811}$ cell account for the continuous capacity fading as depicted in Figure 3d.

2.5. Galvanostatic Cycling Under Exertive Conditions

To fulfill the requirement of achieving a consistent performance when operating over an extended temperature range, in particular for the low-temperature region, a fresh PTNB@Li‖NCM$_{811}$ cell was subjected to 10 cycles (0.3C) at a given temperature spanning from 30 to –10 °C and then reverting the temperature back to 30 °C, with a temperature interval of 10 °C. As demonstrated in **Figure 7a**, following the trend of decreasing operational temperature, the PTNB@Li‖NCM$_{811}$ cell delivers a capacity of 188.8 (30 °C), 180.2 (20 °C), 164.7 (10 °C), 133.1 (0 °C), and 66.4 mAh g^{-1} (–10 °C), respectively. The representative charge-discharge voltage profiles at various temperatures are shown in Figure 7b accordingly. Normalizing based on the capacity delivered at 30 °C (Figure 7c), the cell is still capable of achieving a capacity retention ratio of 70.5 (0 °C) and 35.2% (–10 °C), respectively. By increasing the temperature from –10 to 30 °C (Figure 7a, 7c), the cell manages to recover almost all of the capacity delivered earlier at a given temperature, that is, 131.3 (0 °C) and 164.3 mAh g^{-1} (10 °C). Interestingly, a higher capacity, that is, 182.5 and 194.4 mAh g^{-1}, is attained when increasing the temperature to 20 and 30 °C, respectively. The stable cycling within room-to-low temperature ranges high-lights that the PTNB@Li‖NCM$_{811}$ cell can perform over a broad temperature range.

We further explored the cycling performance of PTNB@Li‖NCM$_{811}$ at a low temperature of 0 °C. The cell was subjected to one formation cycle at 0.05C, followed by 90 cycles at 0.3C (Figure 7d). Initially, a comparatively lower capacity of 163.6 mAh g^{-1} versus 197.7 mAh g^{-1} (20 °C) is supplied, yet this is reasonably high given the fact that most of the cells in quasi-solid electrolyte systems can only perform decently above ambient temperature. Increasing the current density to 0.3C, the cell delivers an initial capacity of 126.5 mAh g^{-1}. Upon the following few cycles, the capacity gradually increases to a max-imum capacity of 136.0 mAh g^{-1}, corresponding to 83.1% of the capacity delivered at 0.05C. After 90 cycles, the cell still retains 121.3 mAh g^{-1} capacity, accounting for 95.9% of the initial capacity. This result confirms that our cell is capable of oper-ating stably for long-term cycling, satisfying the capacity criteria at a low temperature of 0 °C.

From a practical application point of view, the use of thick lithium would not only increase the production cost; it would lower the volumetric/gravimetric energy density. Consequently, researchers have begun to limit the lithium to less than 50 µm in thickness.[70] This provides a realistic performance, neverthe-less, the lack of excess lithium usually leads to poor cycling per-formance.[9] Subsequently, we tried to examine the cell cycling stability under the condition of limited lithium via reducing the lithium thickness from 500 to 20 µm (thin Li deposited on Cu foil). As evidenced in Figure 7e, a slightly lower discharge capacity (ca., 152.3 mAh g^{-1} vs 158.7 mAh g^{-1}) is obtained at 0.5C, yet, the ICE (87.9%) remains the same as what is achieved in the thick lithium system. The capacity remains stable during the initial 50 cycles (Figure 7e, 7f), after which a gradual steady capacity decay is observed upon the following consecutive 150 cycles, ending with a capacity retention ratio of 83.5%. Inter-estingly, the CE of the PTNB@thin Li‖NCM$_{811}$ cell is higher and more stable than that of the PTNB@Li‖NCM$_{811}$ cell. It is worth mentioning that the morphology of thin Li is different from the thick Li foil. The latter shows a rather flat surface (Figure S5a, S5b, Supporting Information) while the former shows submicron-sized nodules (Figure S13, Supporting Infor-mation). Heine et al.[71] showed that electrodes composed of Li powder pressed on Cu foil offer higher CE compared to plain lithium foil electrodes. Overall, the capacity retention of the PTNB@thin Li‖NCM$_{811}$ cell (Figure 7e) is enhanced by 10.3% compared to that of the Li‖NCM$_{811}$ cell (Figure 3d).
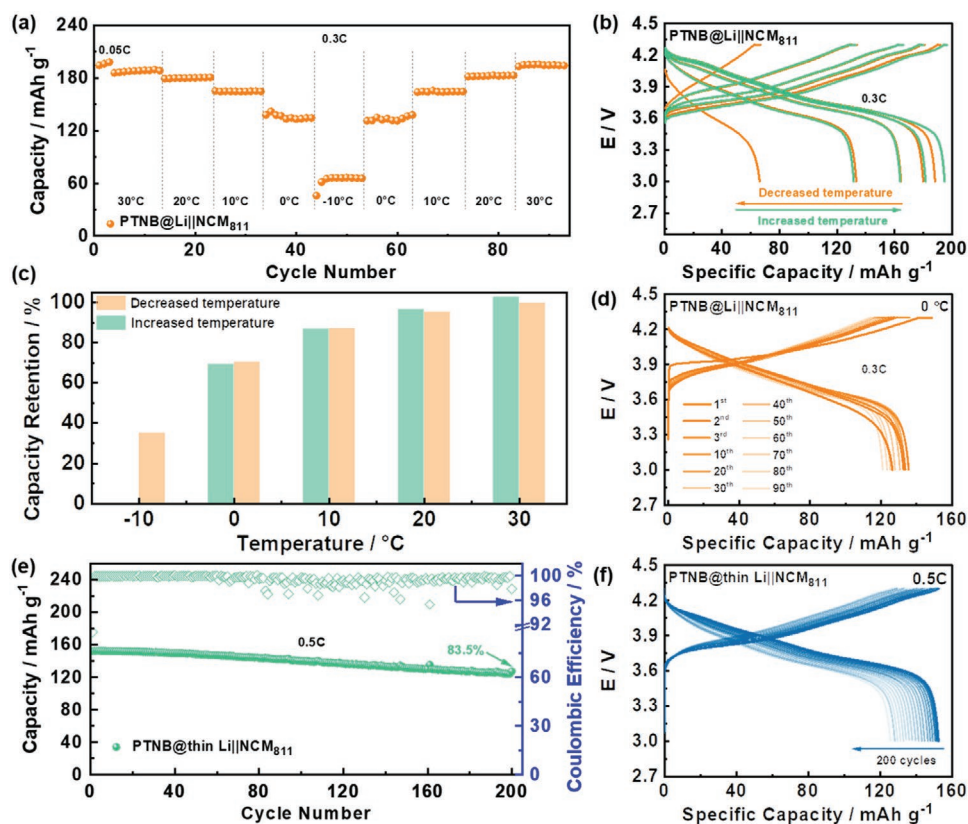
Figure 7. a) Cycling performance of PTNB@Li‖NCM$_{811}$ cell over a wide temperature range (−10–30 °C); b) Representative charge-discharge voltage profiles at selected temperature; c) capacity retention ratio versus temperature plot upon decreasing or increasing the temperature normalized based on the beginning capacity delivered at 30 °C (derived from Figure 7a); d) selected charge-discharge profiles of PTNB@Li‖NCM$_{811}$ cell upon 90 cycles (0.3C, T = 0 °C); e) long-term cycling stability and f) selected charge-discharge voltage profiles (one every 10 cycles) of PTNB@thin Li‖NCM$_{811}$ cell at 0.5C, T = 20 °C.

2.6. Fabrication and Evaluation of Multi-Layer Bipolar Stacking Cells

Unlike the conventional LIBs, the exclusion of free-flowing liquid electrolytes in quasi-SSBs enables the construction of multi-layer bipolar cells. In view of this salient feature, the scope of the investigation was extended to 2-/3-layer bipolar stacking cells. Stainless steel (SUS) is used as the bipolar plate (BP) connecting the NCM$_{811}$ positive electrode of one single unit cell and the lithium negative electrode of the next cell. Figure S14, Supporting Information, shows the charge-discharge voltage profiles of a [(-)SUS|PTNB@Li|hybrid electrolyte|NCM$_{811}$|Al|SUS|PTNB@Li|hybrid electrolyte|NCM$_{811}$|Al|SUS(+)] 2-layer bipolar cell (denoted as B2_PTNB@Li‖NCM$_{811}$). Initially, at 0.05C, a specific discharge capacity of 179.4 mAh g^{-1} is delivered with an ICE of 82.0%. Increasing the current density to 0.1C, the cell still retains 175.9 mAh g^{-1} capacity. After 9 cycles, the capacity steadily increases to 185.2 mAh g^{-1} predominantly due to the gradual electrode activation. However, the capacity starts to decay rapidly since the 10th cycle, leading to only 109.9 mAh g^{-1} capacity remaining after 20 cycles. Although the PTNB@Li‖NCM$_{811}$ mono-polar cell is remarkably stable, any variation between these single-unit cells would cause noticeable performance degradation in bipolar cells. A possible reason for such a strong

capacity decay could be the difference between two NCM$_{811}$ electrodes (i.e., porosity, thickness, uniformity) which could cause different contact with the hybrid film.

To mitigate this impact, a plausible solution is to prepare cathode composites via incorporating 10 wt% of LATP powder (denoted as NCM$_{811}$–C) during the slurry preparation step. These LATP particles act as an extension of ionic pathways to ensure a close contact with NCM$_{811}$ particles and meanwhile enable the filling of pores with LATP particles within positive electrode due to their rather small particle size compared to the NCM$_{811}$ particles. The cycling performance of the [(–)SUS|PTNB@Li|hybrid electrolyte|NCM$_{811}$–C|Al|SUS|PTNB@Li|hybrid electrolyte|NCM$_{811}$–C|Al|SUS(+)] 2-layer bipolar cell (denoted as B2_PTNB@Li‖NCM$_{811}$–C) is shown in **Figure 8a**. Initially, a capacity of 188.7 mAh g^{-1} (0.05C) is achieved with an ICE of 85.3%, which is higher than that of the cell with standard NCM$_{811}$ electrode (179.4 mAh g^{-1}, 82.0%). At 0.1C, a similar capacity augment from 181.8 to 190.9 mAh g^{-1} is observed over 12 cycles, followed by a mild capacity fading to 179.9 mAh g^{-1} in the 20th cycle. Such high capacity retention (ca., 99.0%) demonstrates that the employment of composite positive electrodes is an effective solution to maximally ameliorate the cycling stability of bipolar cells.[72] Subsequently, the feasibility of this strategy in combination with thin lithium (20 µm) in a 2-layer bipolar cell (denoted as B2_PTNB@thin Li‖NCM$_{811}$–C, Figure 8b) was explored.
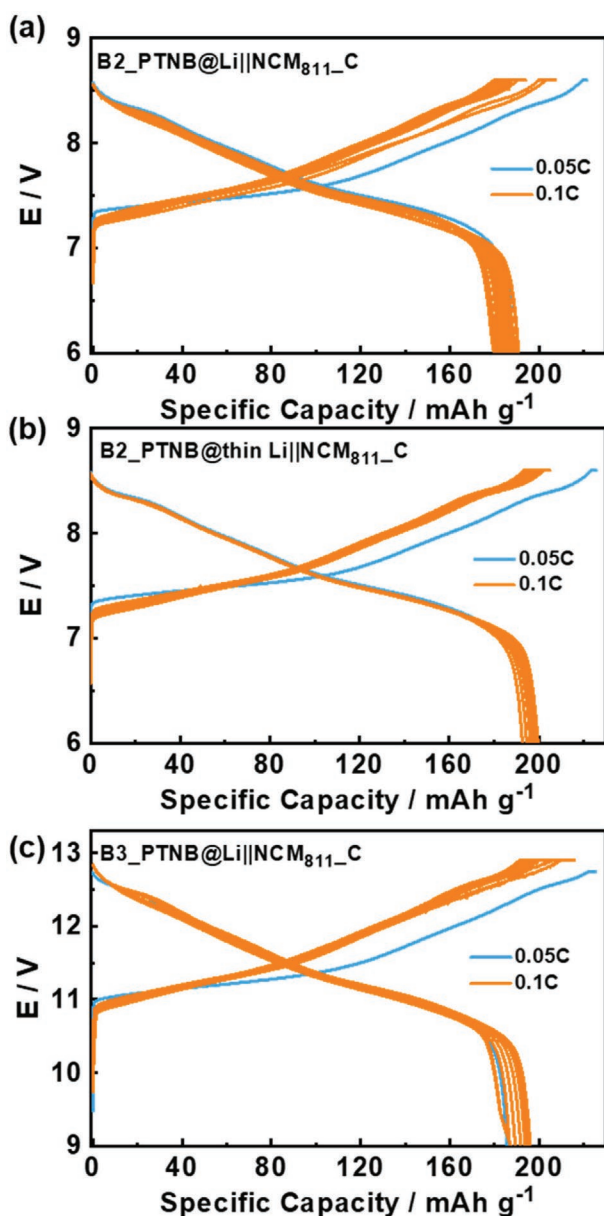
Figure 8. Charge-discharge profiles of a) B2_PTNB@Li||NCM$_{811}$_C (20 cycles), b) B2_PTNB@thin Li||NCM$_{811}$_C (13 cycles), and c) B3_PTNB@Li||NCM$_{811}$_C (10 cycles) cells.

Compared to the thick lithium system, a higher capacity and a higher ICE are achieved at 0.05C, that is, 196.9 mAh g^{-1} and 87.2%. The initial capacity at 0.1C is 192.6 mAh g^{-1} and the capacity reaches a maximum value of 199.5 mAh g^{-1} after 9 cycles, and 196.6 mAh g^{-1} after 13 cycles. An abrupt capacity decay, however, happens in the 14th cycle. Last, we assembled a 3-layer bipolar cell [(–)SUS|PTNB@Li|hybrid electrolyte|NCM$_{811}$_C|Al|SUS|PTNB@Li|hybrid electrolyte|NCM$_{811}$_C|Al|SUS|PTNB@Li|hybrid electrolyte|NCM$_{811}$_C|Al|SUS(+)] (denoted as B3_PTNB@Li||NCM$_{811}$_C). The B3_PTNB@Li||NCM$_{811}$_C cell manages to cycle stably for 10 cycles (Figure 8c), with a maximum capacity of 196.1 mAh g^{-1} (0.1C). Afterward, obvious capacity fading is detected.

To elucidate the possible cause of the sudden capacity deterioration, we opened all the cells and examined the morphology of both negative and positive electrodes. Figure S15a,b and Figure S15e,f, Supporting Information, show the surface morphology of two lithium foils recovered from the cycled B2_PTNB@Li||NCM$_{811}$_C, marked as C_Li_1 and C_Li_2 respectively. It appears that the C_Li_1 sample exhibits a rougher and more uneven surface. Also, some "needle-like" lithium can be observed between the lithium ridges. In comparison, the C_Li_2 sample better preserves the pristine morphology (Figure S5e, S5f, Supporting Information). Regarding the positive electrodes, the surface of the C_NCM$_{811}$_1 sample (Figure S15c, S15d, Supporting Information) is rougher, whereas the C_NCM$_{811}$_2 sample (Figure S15g, S15h, Supporting Information) shows a smoother surface. This implies that C_NCM$_{811}$_1 may have undergone more severe interfacial side reactions. Such a discrepancy (a neat comparison shown in Table S2, Supporting Information) is similarly evidenced in the cycled B2_PTNB@thin Li||NCM$_{811}$_C cell (Figure S16, Table S3, Supporting Information). Specifically, the distribution of lithium nodules within the C_Li_1 is looser than that of the C_Li_2. Meanwhile, the primary particles of the C_NCM$_{811}$_2 demonstrate a rougher surface with some microcracks, which is absent in the sample of the C_NCM$_{811}$_1 sample. With respect to the cycled B3_PTNB@Li||NCM$_{811}$_C cell (Figure S17, Supporting Information), similar to the two previous cases, the morphology of the three sets of negative/positive electrodes is not identical. The detailed comparison is shown in Table S4, Supporting Information. Generally, the NCM$_{811}$ particles in 3-layer bipolar cells display more severely damaged surfaces in contrast to the particles recovered from the 2-layer bipolar cell, reflecting the difficulty of building up more stacked layers. In summary, one common phenomenon is that the variation between each individual unit cell is responsible for the sudden capacity decay. To eliminate this issue, more precise, reliable, and reproducible cell stacking techniques are necessary.

As a "proof-of-concept" study, the results we achieved are already impressive providing the possibility to construct multilayer bipolar cells with high power energy densities. What's more, in both cases, the employment of thin lithium and the increase of stacking layers all lead to reduced cycling stability and shortened lifetime. As a result, to introduce such multilayer bipolar cell prototypes into the market, future efforts demand collaboration from academia and industry to bridge the gap to produce commercially feasible cells.

3. Conclusions

In this work, a thin and flexible hybrid film composed of ion-conducting ceramic LATP, electrochemically inactive PVDF-TrFE polymer, and a small amount of high Li content ILE is fabricated as the composite electrolyte for quasi-solid-state lithium batteries. The "self-extinguishing" and no free-flowing liquid features of this hybrid electrolyte permit a safe operation even under mechanical folding and cutting situations, indicating the high safety property. The presence of a highly concentrated ILE enhances the interfacial contact between electrodes and electrolyte, enabling a moderate cycling lifetime

of $\approx$ 128 h in a Li‖Li symmetric cell, and 112 cycles in a Li‖NCM$_{811}$ cell due to the known chemical instability of LATP against lithium. To address this issue, an interface coating strategy via coating an ultrathin PTNB polymer layer on Li to further isolate their direct contact was adopted. The PTNB interlayer is proved to be very effective in prohibiting the undesired electrode|electrolyte interfacial side reactions, shown by the more than 6 times extended cycling lifetime in PTNB@Li‖PTNB@Li cells with no dendritic lithium found, a reduced and more stable PTNB@Li|LATP interfacial resistances upon cycling in PTNB@Li‖NCM$_{811}$ cells, as well as, thin interphase formation on the surface of both PTNB@Li and NCM$_{811}$. Apart from the effective protection for Li metal, a positive impact on the NCM$_{811}$ electrode side is also evidenced by the better-preserved surface and bulk morphology. Also, the lack of microcrack formation, mitigated structural change, and the stability of hybrid electrolyte|NCM$_{811}$ interfacial resistances all contribute to the significantly enhanced rate capability and extremely stable long-term cycling in PTNB@Li‖NCM$_{811}$ cells.

The investigation of the electrochemical performance of PTNB@Li‖NCM$_{811}$ cells in different exertive scenarios including limited lithium source (20 µm) and a wide temperature range (−10–30 °C) are also included in this work. As a "proof-of-concept" study, we also fabricated bilayer (6.0–8.6 V) and trilayer (9.0–12.9 V) bipolar cells, achieving 20 stable cycles and 10 stable cycles, respectively. The remarkable performance achieved demonstrates that our quasi-solid-state lithium batteries have the potential to meet the requirements for the next-generation lithium batteries with high performance and improved safety profile.

4. Experimental Section

Synthesis of Li$_{1.3}$Al$_{0.3}$Ti$_{1.7}$(PO$_4$)$_3$ (LATP): First, LiCl (Alfa Aesar), Al(NO$_3$)$_3$ 9H$_2$O (Acros Organics), and NH$_4$H$_2$PO$_4$ (EMD Millipore Corporation) were dissolved in distilled water (DIW) with a stoichiometric molar ratio of 1.3:0.3:3 under continuous stirring till a transparent solution was obtained (solution A). Second, solution B was prepared by adding a stoichiometric amount of Ti(C$_4$H$_9$)$_4$ (Sigma-Aldrich) into absolute ethanol (BDH Chemicals) with a weight ratio of 1:1 under stirring until a homogenous solution was obtained. Afterward, solution B was added into solution A slowly to form a white color suspension, which was kept for 2 h under continuous stirring at ambient temperature. The suspension was then ball-milled with ZrO$_2$ balls for 24 h. The LATP precursor powder was collected by a rotary evaporator (60 °C) and a further drying step (80 °C) in an oven. To obtain the final LATP product, the precursor was pre-heated at 400 °C for 4 h, and further calcined at 950 °C for 12 h. To destroy the possible aggregation of LATP particles, the powders were manually ground in an agate mortar before usage.

Preparation of LATP/PVDF-TrFE Film: The flexible LATP/PVDF-TrFE film was prepared by a phase inversion process.[73] Polyvinylidenefluoride-trifluoroethylene (PVDF-TrFE; PolyK Technologies) polymer was first dissolved in N-methyl-2-pyrrolidone (NMP; Alfa Aesar). LATP powder, PVDF-TrFE/NMP, and acetone were mixed in a mixer (NBK-1 Non-Bubbling Kneader) at ambient temperature for 15 min to get a homogenous slurry. The weight ratio of LATP and PVDF-TrFE was 92:8. The slurry was then cast on a glass plate via doctor blade technique. The film was transferred into a container filled with DIW and kept for 20 min. The film was then pre-dried in the dry room (dew point ←60 °C) and further vacuum dried at 80 °C for 10 h. To obtain a thin and compact film, the dry LATP/PVDF-TrFE hybrid film was eventually subjected to a hot calendaring step at 50 °C.

Preparation of LATP/PVDF-TrFE/ILE Hybrid Film: The LATP/PVDF-TrFE/ILE hybrid electrolyte was prepared by adding ≈100 µL of ILE (0.4LiFSI-0.6Pyr$_{14}$FSI) into the as-prepared LATP/PVDF-TrFE film (≈ 1.5 cm × 2 cm) and then applying a vacuum step for a few minutes to allow for better film wetting. The excess ILE was squeezed to avoid any free-flowing liquid electrolyte.

Synthesis of Poly[2,3-Bis(2,2,6,6-Tetramethylpiperidine-N-Oxycarbonyl)-Norbornene] (PTNB): To 300 mL of a dry benzene (Aldrich) solution of *cis*-5-norbornene-*endo*-2,3-dicarboxylic anhydride (Aldrich) were added 4-hydroxy-2,2,6,6-tetramethylpiperidinyl-*N*-oxy (Aldrich), *N,N*-dimethylaminopyridine (Aldrich), and trimethylamine (Aldrich), and the mixture was stirred for 12 h at 80 °C under nitrogen and then cooled to room temperature. 2-Chloro-1-methylpyridinium iodide (Aldrich) was added to the reaction mixture, which was vigorously stirred for 12 h at room temperature. The precipitate (the residue of 2-chloro-1-methylpyridinium iodide) was removed by filtration, and triethylamine was removed in vacuum. The crude product was extracted with chloroform (DAEJUNG), washed with an aqueous solution of ammonium chloride (DAEJUNG), and dried over anhydrous magnesium sulfate (DAEJUNG). The solvent was removed in vacuum, and the residue was purified using a silica gel column with an ethyl acetate/chloroform/hexane (1/6/3) eluent (DAEJUNG). Two diastereomers, the *endo-*, *endo-* and *endo-*, *exo*-derivatives, were isolated as orange crystals by recrystallization from hexane/chloroform (DAEJUNG). To a 1.0 mL toluene (DAEJUNG) solution of the monomer was added the Grubbs second-generation catalyst (Alfa), and the mixture was stirred for 12 h at 40 °C under an argon atmosphere. The polymerization mixture was poured into hexane (DAEJUNG), and the precipitated polymer powder was purified by reprecipitation from chloroform into diethyl ether (Aldrich) to form a pale orange powder.

Preparation of PTNB Coated Li Metal (PTNB@Li): PTNB powder was dissolved in 1,2-dimethoxyethane (DME; Sigma-Aldrich) with concentrations of 0.4, 1, and 2 wt%, respectively. A piece of Li metal (Honjo, 500 µm) or Li deposited on copper (Honjo, 20 µm) was immersed into the above solutions for 4 min, afterwards, the samples were vacuum dried immediately to remove the DME solvent. Then the PTNB coated Li was prepared with a total preparation time of approximately 7 min.

Material Characterizations: The crystallinity of LATP powder was characterized by XRD (Bruker D8 with Cu Kα radiation, λ = 0.15406 nm). The morphology of all samples (powders, films, and electrodes) was examined by SEM (ZEISS EVO MA 10 microscope). The investigation of the cross-sectional view of cycled NCM$_{811}$ particles was performed using a FIB coupled with SEM. The thermal stability of pure PVDF-TrFE polymer, pure LATP powder, LATP/PVDF-TrFE film, and LATP/PVDF-TrFE/ILE hybrid film was evaluated by TGA (Discovery TGA, TA instruments). After an isothermal step (40 °C, 30 min), samples were heated up to 700 °C at a heating rate of 3 °C min^{-1} in an artificial air atmosphere (flow rate ratio of N$_2$ and O$_2$ was fixed at 60:40). The ionic conductivity of ILE (20 °C) was determined using a conductivity meter (Biologic MCS-10). The ionic conductivity of LATP/PVDF-TrFE/ILE (20 °C) was determined by using a frequency response analyzer (Solartron 1260). XPS measurements were performed using a monochromatic Al Kα (hν = 1,487 eV) X-ray source and a Phoibos 150 XPS spectrometer (SPECS–Surface concept) equipped with a micro-channel plate and Delay Line Detector (DLD). The scans were acquired in a Fixed Analyzer Transmission mode with an X-ray power source of 200 W (15 kV), 30 eV pass energy, and 0.1 eV energy steps. The depth profiling was performed by a focused ion gun for 5 keV Ar$^+$ with an ion filter and sputtering rate of 0.8 nm min^{-1}. The CasaXPS software was used for the spectra fitting, using a nonlinear Shirley-type background and 70% Gaussian and 30% Lorentzian profile functions.[74] For ex situ SEM, FIB, TEM (FEI Titan 80–300, 300 kV), and XPS investigations, cycled cells (200 cycles at 0.5C) were opened in the dry room. Recovered positive and negative electrodes were washed with dimethyl carbonate (DMC) solvent, and vacuum dried in Büchi to remove any residual solvent and ILE. Samples were transferred by home-designed air-tight SEM, TEM, and XPS transfer box to avoid any contact with moist air.

Electrode Preparation and Cell Assembly: The NCM$_{811}$ positive electrodes were prepared by mixing NCM$_{811}$ (92 wt%; POSCO), C-NERGY Super C65 (4 wt%; TIMCAL), poly(vinylidene difluoride) (PVDF 6020, 4 wt%; Solvay,) and NMP (Aldrich) using a mixer for 15 min. The solid:liquid weight ratio was fixed at 1:1. The homogenous slurries were then cast on Al foils by a doctor-blade technique. Prior to the vacuum drying step (glass oven B-585 Drying, Büchi, 100 °C for 12 h), the wet electrode sheets were pre-dried at 60 °C to remove NMP and then punched into disks with a diameter of 12 mm. The NCM$_{811}$ composite positive electrodes were prepared in the same way, except the weight ratio between each component was fixed at 82:10:4:4 (NCM$_{811}$:LATP:Super C65:PVDF). The average active material loading density of both positive electrodes was controlled to be ≈2.5 ± 0.1 mg cm^{-2}. All the specific capacities were calculated based on the mass of NCM$_{811}$. All the processes were performed in the dry room with a dew point always below −60 at 20 °C.

All mono-polar cells (Li‖NCM$_{811}$) were assembled in two-electrode pouch cells comprising of NCM$_{811}$ as the positive electrode, lithium metal as the negative electrode, and LATP/PVDF-TrFE/ILE as the hybrid electrolyte. The voltage range was set between 3.0 and 4.3 V and the current density at 1C was set to be 200 mA g^{-1}. The symmetric cells (Li‖Li) for the lithium stripping-plating test were also prepared in two-electrode pouch cells. The current density was fixed at 0.1 mA cm^{-2} and the areal capacity for each stripping-plating cycle was fixed at 0.2 mAh cm^{-2}. The ESW of the LATP/PVDF-TrFE/ILE hybrid electrolyte, and the cathodic scans of various ILE (0.3LiFSI-0.7Pyr$_{14}$FSI, 0.4LiFSI-0.6Pyr$_{14}$FSI, and 0.5LiFSI-0.5Pyr$_{14}$FSI) were determined in two-electrode Swagelok cells using reversible lithium and ion-blocking electrodes, ca., Li metal‖stainless steel (Li‖SS). The ESW of the PTNB and the electrolytes were determined in coin cells using lithium and a blocking electrode, for example, Li metal‖Al (Li‖Al) for the anodic scan and Li metal‖Cu (Li‖Cu) for the cathodic scan. The bipolar stacked cells were also assembled in two-electrode Swagelok cells. The voltage range for 2-layer and 3-layer bipolar stacking cells was set to 6.0–8.6 V and 9.0–12.9 V, respectively. To facilitate the understanding of different components in several cell configurations discussed in this work, here a schematic illustration of all types of cells is provided in Figure S18, Supporting Information.

Electrochemical Characterizations: All the electrochemical performance tests were conducted using a battery tester (Maccor series 4000). A climatic chamber (Binder GmbH) was used to control the cell operation temperature. For the long-term cycling performance test, cells were always activated by one formation cycle at 0.05C and three formation cycles at 0.1C before subjecting to higher constant C-rates, that is, 0.3C (0 °C) and 0.5C (20 °C). The EIS (frequency range: 100 kHz–10 mHz; AC amplitude: 10 mV) upon galvanostatic cycling were recorded using a multi-channel potentiostat (VMP Biologic-Science Instruments). The impedances at de-/lithiation state were always recorded after a constant voltage step (10 min). The cycling performance of bipolar cells was also conducted in the multi-channel potentiostat (VMP Biologic-Science Instruments).

Supporting Information

Supporting Information is available from the Wiley Online Library or from the author.

Acknowledgements

Conflict of Interest

The authors declare no conflict of interest.

Data Availability Statement

Research data are not shared.

Keywords

[1] J. M. Tarascon, M. Armand, *Nature* **2001**, *414*, 359.
[2] M. S. Whittingham, *MRS Bull.* **2008**, *33*, 411.
[3] M. S. Whittingham, *Chem. Rev.* **2004**, *104*, 4271.
[4] Z. Chen, G.-T. Kim, Z. Wang, D. Bresser, B. Qin, D. Geiger, U. Kaiser, X. Wang, Z. X. Shen, S. Passerini, *Nano Energy* **2019**, *64*, 103986.
[5] X. Feng, M. Ouyang, X. Liu, L. Lu, Y. Xia, X. He, *Energy Storage Mater.* **2018**, *10*, 246.
[6] M. Armand, J. M. Tarascon, *Nature* **2008**, *451*, 652.
[7] T.-H. Kim, J.-S. Park, S. K. Chang, S. Choi, J. H. Ryu, H.-K. Song, *Adv. Energy Mater.* **2012**, *2*, 860.
[8] A. Manthiram, X. Yu, S. Wang, *Nat. Rev. Mater.* **2017**, *2*, 16103.
[9] R. Weber, M. Genovese, A. J. Louli, S. Hames, C. Martin, I. G. Hill, J. R. Dahn, *Nat. Energy* **2019**, *4*, 683.
[10] J. Betz, G. Bieker, P. Meister, T. Placke, M. Winter, R. Schmuch, *Adv. Energy Mater.* **2019**, *9*, 1803170.
[11] S. Xin, Y. You, S. Wang, H.-C. Gao, Y.-X. Yin, Y.-G. Guo, *ACS Energy Lett.* **2017**, *2*, 1385.
[12] J. Wu, L. Yuan, W. Zhang, Z. Li, X. Xie, Y. Huang, *Energy Environ. Sci.* **2021**, *14*, 12.
[13] A. Perea, M. Dontigny, K. Zaghib, *J. Power Sources* **2017**, *359*, 182.
[14] Y. Tian, T. Shi, W. D. Richards, J. Li, J. C. Kim, S.-H. Bo, G. Ceder, *Energy Environ. Sci.* **2017**, *10*, 1150.
[15] K. N. Jung, H. S. Shin, M. S. Park, J. W. Lee, *ChemElectroChem* **2019**, *6*, 3842.
[16] H.-S. Shin, W.-G. Ryu, M.-S. Park, K.-N. Jung, H. Kim, J.-W. Lee, *ChemSusChem* **2018**, *11*, 3184.
[17] Y. He, C. Lu, S. Liu, W. Zheng, J. Luo, *Adv. Energy Mater.* **2019**, *9*, 1901810.
[18] H. Shen, E. Yi, L. Cheng, M. Amores, G. Chen, S. W. Sofie, M. M. Doeff, *Sustainable Energy Fuels* **2019**, *3*, 1647.
[19] R. DeWees, H. Wang, *ChemSusChem* **2019**, *12*, 3713.
[20] P. Hartmann, T. Leichtweiss, M. R. Busche, M. Schneider, M. Reich, J. Sann, P. Adelhelm, J. Janek, *J. Phys. Chem. C* **2013**, *117*, 21064.
[21] Y. Liu, C. Li, B. Li, H. Song, Z. Cheng, M. Chen, P. He, H. Zhou, *Adv. Energy Mater.* **2018**, *8*, 1702374.
[22] Q. Cheng, A. Li, N. Li, S. Li, A. Zangiabadi, W. Huang, A. C. Li, T. Jin, Q. Song, W. Xu, *Joule* **2019**, *3*, 1510.
[23] L. Yang, Y. Song, H. Liu, Z. Wang, K. Yang, Q. Zhao, Y. Cui, J. Wen, W. Luo, F. Pan, *Small Methods* **2020**, *4*, 1900751.
[24] Y. Liu, Q. Sun, Y. Zhao, B. Wang, P. Kaghazchi, K. R. Adair, R. Li, C. Zhang, J. Liu, L.-Y. Kuo, *ACS Appl. Mater. Interfaces* **2018**, *10*, 31240.

[25] X. Hao, Q. Zhao, S. Su, S. Zhang, J. Ma, L. Shen, Q. Yu, L. Zhao, Y. Liu, F. Kang, Y.-B. He, *Adv. Energy Mater.* **2019**, *9*, 1901604.

[26] W. Zhou, S. Wang, Y. Li, S. Xin, A. Manthiram, J. B. Goodenough, *J. Am. Chem. Soc.* **2016**, *138*, 9385.

[27] S. Yu, S. Schmohl, Z. Liu, M. Hoffmeyer, N. Schön, F. Hausen, H. Tempel, H. Kungl, H. D. Wiemhöfer, R. A. Eichel, *J. Mater. Chem. A* **2019**, *7*, 3882.

[28] Z. Yang, H. Yuan, C. Zhou, Y. Wu, W. Tang, S. Sang, H. Liu, *Chem. Eng. J.* **2020**, *392*, 123650.

[29] Y. Wang, Q. Zhang, Z.-C. Xue, L. Yang, J. Wang, F. Meng, Q. Li, H. Pan, J.-N. Zhang, Z. Jiang, W. Yang, X. Yu, L. Gu, H. Li, *Adv. Energy Mater.* **2020**, *10*, 2001413.

[30] J. Liu, T. Liu, Y. Pu, M. Guan, Z. Tang, F. Ding, Z. Xu, Y. Li, *RSC Adv.* **2017**, *7*, 46545.

[31] W. C. West, J. F. Whitacre, J. R. Lim, *J. Power Sources* **2004**, *126*, 134.

[32] H.-S. Kim, Y. Oh, K. H. Kang, J. H. Kim, J. Kim, C. S. Yoon, *ACS Appl. Mater. Interfaces* **2017**, *9*, 16063.

[33] X. Yu, A. Manthiram, *ACS Appl. Energy Mater.* **2020**, *3*, 2916.

[34] T. Yoshinari, R. Koerver, P. Hofmann, Y. Uchimoto, W. G. Zeier, J. Janek, *ACS Appl. Mater. Interfaces* **2019**, *11*, 23244.

[35] M. Keller, A. Varzi, S. Passerini, *J. Power Sources* **2018**, *392*, 206.

[36] M. R. Busche, T. Drossel, T. Leichtweiss, D. A. Weber, M. Falk, M. Schneider, M.-L. Reich, H. Sommer, P. Adelhelm, J. Janek, *Nat. Chem.* **2016**, *8*, 426.

[37] Z. Chen, G.-T. Kim, D. Bresser, T. Diemant, J. Asenbauer, S. Jeong, M. Copley, R. J. Behm, J. Lin, Z. Shen, S. Passerini, *Adv. Energy Mater.* **2018**, *8*, 1801573.

[38] J.-H. Shin, W. A. Henderson, S. Passerini, *Electrochem. Commun.* **2003**, *5*, 1016.

[39] G. -T. Kim, G. B. Appetecchi, M. Montanino, F. Alessandrini, S. Passerini, *ECS Trans.* **2010**, *25*, 127.

[40] I. Osada, H. de Vries, B. Scrosati, S. Passerini, *Angew. Chem., Int. Ed.* **2016**, *55*, 500.

[41] S. A. Pervez, G. Kim, B. P. Vinayan, M. A. Cambaz, M. Kuenzel, M. Hekmatfar, M. Fichtner, S. Passerini, *Small* **2020**, *16*, 2000279.

[42] S.-K. Jeong, H.-Y. Seo, D.-H. Kim, H.-K. Han, J.-G. Kim, Y. B. Lee, Y. Iriyama, T. Abe, Z. Ogumi, *Electrochem. Commun.* **2008**, *10*, 635.

[43] D. A. Rakov, F. Chen, S. A. Ferdousi, H. Li, T. Pathirana, A. N. Simonov, P. C. Howlett, R. Atkin, M. Forsyth, *Nat. Mater.* **2020**, *19*, 1096.

[44] H. Zhang, W. Qu, N. Chen, Y. Huang, L. Li, F. Wu, R. Chen, *Electrochim. Acta* **2018**, *285*, 78.

[45] C. A. Nguyen, S. Xiong, J. Ma, X. Lu, P. S. Lee, *Phys. Chem. Chem. Phys.* **2011**, *13*, 13319.

[46] A. Arshad, M. Wahid, M. Rusop, W. Majid, R. Subban, M. Rozana, *J. Nanomater.* **2019**, *2019*, 5961563.

[47] L. Xu, F. Yang, C. Su, L. Ji, C. Zhang, *Electrochim. Acta* **2014**, *130*, 148.

[48] C. Karlsson, T. Suga, H. Nishide, *ACS Appl. Mater. Interfaces* **2017**, *9*, 10692.

[49] H. Nishide, K. Koshika, K. Oyaizu, *Pure Appl. Chem.* **2009**, *81*, 1961.

[50] J.-K. Kim, Y. Kim, S. Park, H. Ko, Y. Kim, *Energy Environ. Sci.* **2016**, *9*, 1264.

[51] H. W. Kim, H.-J. Kim, H. Byeon, J. Kim, J. W. Yang, Y. Kim, J.-K. Kim, *J. Mater. Chem. A* **2020**, *8*, 17980.

[52] G. B. Appetecchi, M. Montanino, A. Balducci, S. F. Lux, M. Winter, S. Passerini, *J. Power Sources* **2009**, *192*, 599.

[53] M. Moreno, E. Simonetti, G. Appetecchi, M. Carewska, M. Montanino, G.-T. Kim, N. Loeffler, S. Passerini, *J. Electrochem. Soc.* **2016**, *164*, A6026.

[54] Z. Chen, D. Steinle, H.-D. Nguyen, J.-K. Kim, A. Mayer, J. Shi, E. Paillard, C. Iojoiu, S. Passerini, D. Bresser, *Nano Energy* **2020**, *77*, 105129.

[55] M. Gaberscek, J. Moskon, B. Erjavec, R. Dominko, J. Jamnik, *Electrochem. Solid-State Lett.* **2008**, *11*, A170.

[56] A. Birrozzi, N. Laszczynski, M. Hekmatfar, J. von Zamory, G. A. Giffin, S. Passerini, *J. Power Sources* **2016**, *325*, 525.

[57] L. Wang, J. Zhao, X. He, J. Gao, J. Li, C. Wan, C. Jiang, *Int. J. Electrochem. Sci.* **2012**, *7*, 345.

[58] A. M. Andersson, A. Henningson, H. Siegbahn, U. Jansson, K. Edström, *J. Power Sources* **2003**, *119*, 522.

[59] J. F. Moulder, W. Stickle, P. Sobol, K. Bomben, Handbook of X-ray Photoelectron Spectroscopy, Perkin-Elmer Corporation, Eden Prairie, MN, USA **1992**.

[60] K. N. Wood, E. Kazyak, A. F. Chadwick, K.-H. Chen, J.-G. Zhang, K. Thornton, N. P. Dasgupta, *ACS Cent. Sci.* **2016**, *2*, 790.

[61] X-ray Photoelectron Spectroscopy (XPS) Oxygen 1s, http://www.xps-fitting.com/search/label/Oxygen (accessed: September 2020).

[62] C. Wagner, W. Riggs, L. Davis, J. Moulder, G. Muilenberg, Handbook of X-ray Photoelectron Spectroscopy, Physical Electronics Division, Eden Prairie, Minn **1979**, 55344.

[63] H. Kim, F. Wu, J. T. Lee, N. Nitta, H. T. Lin, M. Oschatz, W. I. Cho, S. Kaskel, O. Borodin, G. Yushin, *Adv. Energy Mater.* **2015**, *5*, 1401792.

[64] E. Markevich, G. Salitra, A. Rosenman, Y. Talyosef, F. Chesneau, D. Aurbach, *J. Mater. Chem. A* **2015**, *3*, 19873.

[65] H.-H. Ryu, K.-J. Park, C. S. Yoon, Y.-K. Sun, *Chem. Mater.* **2018**, *30*, 1155.

[66] J.-M. Lim, T. Hwang, D. Kim, M.-S. Park, K. Cho, M. Cho, *Sci. Rep.* **2017**, *7*, 39669.

[67] Q. Liu, W. Zheng, Z. Lu, X. Zhang, K. Wan, J. Luo, J. Fransaer, *ChemSusChem* **2020**, *13*, 3237.

[68] Z. Chen, G.-T. Kim, Y. Guang, D. Bresser, T. Diemant, Y. Huang, M. Copley, R. J. Behm, S. Passerini, Z. Shen, *J. Power Sources* **2018**, *402*, 263.

[69] Z. Chen, Z. Wang, G.-T. Kim, G. Yang, H. Wang, X. Wang, Y. Huang, S. Passerini, Z. Shen, *ACS Appl. Mater. Interfaces* **2019**, *11*, 26994.

[70] J. Liu, Z. Bao, Y. Cui, E. J. Dufek, J. B. Goodenough, P. Khalifah, Q. Li, B. Y. Liaw, P. Liu, A. Manthiram, Y. S. Meng, V. R. Subramanian, M. F. Toney, V. V. Viswanathan, M. S. Whittingham, J. Xiao, W. Xu, J. Yang, X.-Q. Yang, J.-G. Zhang, *Nat. Energy* **2019**, *4*, 180.

[71] J. Heine, S. Krüger, C. Hartnig, U. Wietelmann, M. Winter, P. Bieker, *Adv. Energy Mater.* **2014**, *4*, 1300815.

[72] X. Chen, W. He, L.-X. Ding, S. Wang, H. Wang, *Energy Environ. Sci.* **2019**, *12*, 938.

[73] K. Kimmerle, H. Strathmann, *Desalination* **1990**, *79*, 283.

[74] J. Walton, P. Wincott, N. Fairley, A. Carrick, *Peak Fitting with CasaXPS: A Casa Pocket Book* **2010**.